Table 1: Structural Statistics for CwlCr[a]

total no. of distance constraints	1206
long-range ($\|i-j\| > 4$)	361
middle-range ($\|i-j\| = 2, 3,$ or 4)	232
short-range ($\|i-j\| = 1$)	276
intraresidue	265
hydrogen bond constraints	36 × 2
no. of dihedral constraints	
ϕ, φ	58, 58
χ_1	18
residual dipole couplings $^1D_{NH}$	63
rms deviation from experimental constraints[b]	
distance (Å)	0.0291 ± 0.0005
angle (deg)	0.78 ± 0.03
$^1D_{NH}$ (Hz)	0.63 ± 0.01
rms deviation from idealized covalent geometry	
bonds (Å)	$0.0023 \pm 5 \times 10^{-5}$
angles (deg)	0.434 ± 0.004
impropers (deg)	0.330 ± 0.006
CNS energy terms (kcal/mol)	
E_{bond}	6.1 ± 0.2
E_{angle}	62 ± 1
E_{imp}	9.7 ± 0.4
E_{vdw}[c]	−193 ± 8
PROCHECK Ramachandran plot (residues 185−254)	
residues in most favored regions (%)	95.4
residues in additional allowed regions (%)	4.2
residues in generously allowed regions (%)	0.1
residues in disallowed regions (%)	0.3
rms deviation of mean structure derived from 30 calculated structures	
backbone atoms (residues 185−254) (Å)	0.16
all heavy atoms (residues 185−254) (Å)	0.52

[a] These statistics comprise the ensemble of the 30 lowest-energy structures obtained from 100 starting structures. Structure calculations were performed using CNS version 1.1. [b] None of these structures exhibited distance violations of >0.4 Å, dihedral angle violations of >5°, or residual $^1D_{NH}$ dipolar coupling violations of >2 Hz. [c] E_{vdw} is the Lennard-Jones energy of CNS energy terms.

angles derived from TALOS were also used in the final refinement step (*29*). The χ_1 rotomer of the side chains was estimated from HNHB and HN(CO)HB experiments (*30*, *31*). Residual $^1D_{NH}$ couplings were extracted from the difference in *J* splittings measured for isotropic and anisotropic samples. The *J* splittings for $^{15}N-^1H$ were obtained from 2D $^1H-^{15}N$ IPAP experiments performed in an interleaved manner (*32*). All NMR spectra were analyzed using Sparky (*21*).

CYANA version 1.05 with the CANDID protocol was used for the purposes of structural restraint collection (*33*). Finally, an ensemble of 100 CwlCr structures was calculated using CNS version 1.1 with residual $^1D_{NH}$ couplings by a standard simulated annealing protocol (*34*). Initial estimation for the axial component of the molecular alignment tensor (D_a) and the rhombicity (R) were obtained on the basis of the structure calculated with CYANA using PALES (*35*). These values were optimized in an iterative manner, using the structures calculated by CNS. The final values of D_a and R were 6.28 Hz and 0.32, respectively. The final 30 lowest-energy ensemble structures were checked by PROCHECK-NMR (*36*), and graphics were created with MOLMOL (*37*).

NMR Spectroscopy of CwlCr21. Multidimensional NMR spectroscopy for CwlCr21 was performed essentially as described for CwlCr. Briefly, HNCACB, HN(CO)CACB, HN(CA)CO, and HNCO experiments for main chain resonance assignments were performed on the DRX800 instrument (*22*, *23*). HN(CO-TOCSY)NH and $^{h3}J_{NC'}$HNCO experiments were performed on the AVANCE 500 instrument (*25*, *27*, *28*).

Chemical Shift Perturbation Experiments. Soluble digested peptidoglycan was prepared by enzymatic digestion of purified peptidoglycan from vegetative cells of *B. subtilis* with intact CwlC. The reaction that was employed was carried out essentially according to the published procedure (*15*). Recombinant CwlC enzyme and purified peptidoglycan were prepared essentially as previously described (*15*). Chemically synthesized building blocks of peptidoglycan, (1) diaminopimelic acid (DL-α,ε-diaminopimelic acid), (2) Ala-D-γ-Glu-Lys-D-Ala-D-Ala, (3) GlcNAc [*N*-acetyl-D-(+)-glucosamine], and (4) GlcNAcMurNAcAlaGln [*N*-acetyl-D-glucosaminyl-β-(1,4)-*N*-acetylmuramyl-L-alanyl-D-isoglutamine], were purchased from SIGMA or Wako.

^1H and ^{15}N amide resonance changes in uniformly ^{15}N-labeled CwlCr were monitored following the addition of a large excess of additives to 20 mM HEPES buffer (pH 6.9) containing 0.1 mM CwlCr, 20 mM KCl, 1 mM EDTA, and 5% ^2H_2O. The ratio of the diaminopimelic acid, Ala-D-γ-Glu-Lys-D-Ala-D-Ala, GlcNAc, and GlcNAcMurNAcAlaGln to CwlCr was 100:100:100:10. CwlC-digested peptidoglycan could be dissolved in an aqueous solution up to 0.5 mg/mL, and the perturbation experiment was performed with 0.5 mg/mL digested peptidoglycan. MALDI-TOF MS analysis of the major fragments of the digested products showed multiplets around 158 × 10^2. The $^1H-^{15}N$ HSQC spectra were obtained at 30 °C. For each cross-peak, the normalized weighted average shift difference, $\delta_{ave}/\delta_{max}$, was calculated (*38*, *39*). The weighted average shift difference, δ_{ave}, was calculated as $[\delta^1{}_H{}^2 + (\delta^{15}{}_N)^2/25]^{1/2}$, where $\delta^1{}_H$ and $\delta^{15}{}_N$ represent the difference in parts per million between the free and perturbed chemical shifts. The δ_{max} value represents the maximum observed weighted average shift difference. Changes in signal intensity were also evaluated using the ratio of the intensity difference caused by perturbation and the reference spectrum, $(I_{ref} - I_{per})/I_{ref}$, where I_{ref} and I_{per} represent the signal intensity of the reference and perturbed spectrum, respectively.

RESULTS AND DISCUSSION

Structure Determination. Isotopically labeled recombinant CwlCr (residues 177−255) was overexpressed in *E. coli* and purified by affinity tag and ion-exchange chromatography. The protein obtained was able to bind peptidoglycan (data not shown). The $^{15}N-^1H$ HSQC spectrum in Figure 2 shows highly dispersed cross-peaks, suggesting that CwlCr adopts a stable tertiary structure in solution.

NMR resonance assignments were obtained by performing double- and triple-resonance NMR experiments using ^{15}N-labeled and ^{15}N- and ^{13}C-labeled protein samples. Almost all of the main chain resonance assignments were obtained from the HNCACB, HN(CO)CACB, HN(CA)CO, and HNCO spectra. In this process, the sequential walk was confirmed by the well-dispersed amide ^{15}N and ^1H chemical shifts obtained from the 3D (H)N(CO-TOCSY)-NH experiment, where the magnetization transfer pathway was not through space but through the bonds, with $^1HN \rightarrow {}^{15}N(t_1) \rightarrow {}^{13}C' \rightarrow$ isotropic mixing $\rightarrow {}^{13}C' \rightarrow {}^{15}N(t_2) \rightarrow {}^1HN(t_3)$. This experiment provided the correlation between amide $N(n \pm 1)$ and $N(n)$ and $HN(n)$. $\omega_3(^1H)/\omega_1(^{15}N)$ strips taken through the ^{15}N diagonal peaks in the $\omega_1(^{15}N)/\omega_2(^{15}N)$ plane displayed sequential amide−amide connectivity (Figure 3).

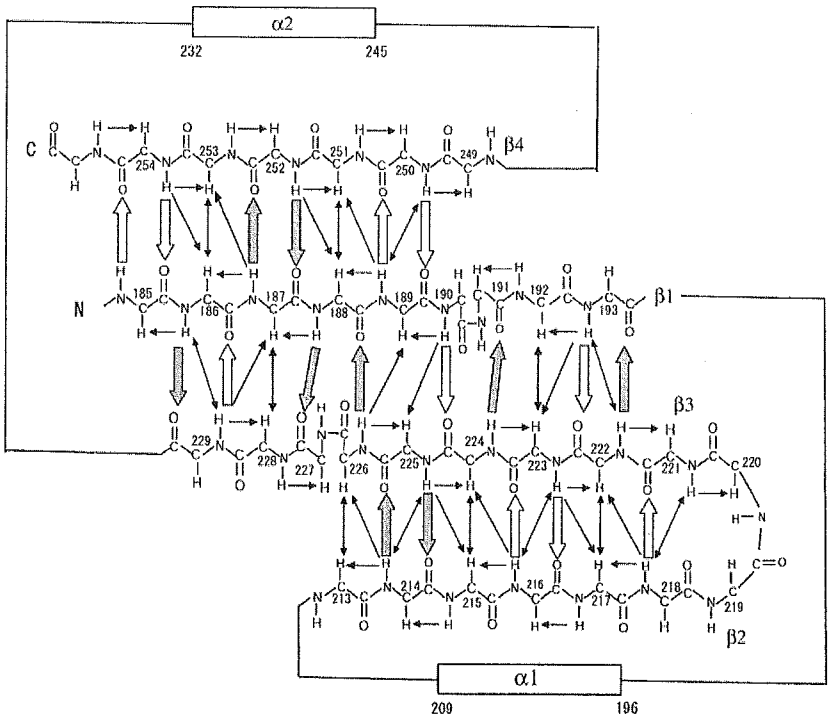

FIGURE 4: Schematic diagram of CwlCr secondary structure. The hydrogen bonds identified through scalar couplings across hydrogen bonds ($^{h3}J_{NC'}$) are displayed as wide arrows. Gray wide arrows represent hydrogen bonds observed in both CwlCr and CwlCr21 (see the text). The Y186 NH:F229 C′, K187 NH:L252 C′, V188 NH:G227 C′, I214 NH:Q225 C′, Y222 NH:F193 C′, V224 NH:G191 C′, I226 NH:V188 C′, Q225 NH:214 C′, and L252 NH:K187 C′ hydrogen bonds of CwlCr correspond to the Y3 NH:F46 C′, K4 NH:L69 C′, V5 NH:G44 C′, I31 NH:Q42 C′, Y39 NH:F10 C′, V41 NH:G8 C′, I43 NH:V5 C′, Q42 NH:I31 C′, and L69 NH:K 4C′ hydrogen bonds of CwCr21, respectively. The observed NOEs are represented with thin arrows. For simplicity, two α-helices are represented with white boxes.

Given the highly conserved repeated sequences within CwlCr, the chemical shifts of symmetrically positioned atoms were similar to each other, in particular, the two turn regions, I190, G191, A192, and F193 in repeat 1 and I226, G227, A228, and F229 in repeat 2 with identical amino acid sequence, where the Cα, Cβ, and C′ resonances of A192 and those of A228 were very similar to each other. Sequential assignment of these regions was clearly verified by the amide correlations obtained from the 3D (H)N(CO-TOCSY)-NH experiment, which provided the unambiguous sequential walk (Figure 3). Some peaks displayed longer-range connectivity, and these were valuable for establishing reliable assignments.

The side chain assignments were mainly obtained from the 3D C(CO)NH, H(CCO)NH, HCCH-TOCSY, and 4D HC(CO)NH spectra. Combined use of the 3D HCCH-TOCSY spectra with the 4D HC(CO)NH spectra enabled us to obtain unambiguous correlations between side chain ^{13}C and ^{1}H nuclei, which allowed for reliable side chain assignments. In an effort to obtain precise structural information, all of the methyl groups of leucine and valine were stereospecifically assigned using randomly 15% ^{13}C-enriched protein.

The structure of CwlCr was determined from 1206 distance and 134 torsion angle restraints (Table 1). This relatively large number of angle restraints was due to the φ and χ_1 angles obtained from TALOS, and the HNHB and HN(CO)-HB experiments, respectively. Furthermore, a total of 36 hydrogen bonds detected directly via $^{h3}J_{NC'}$ couplings were used as restraints (Figure 4). Of these, both the β-sheet and α-helices each possessed 18 hydrogen bonds. The direct observation of hydrogen bonds was extremely useful in the initial structure determination steps, since they facilitated the unambiguous determination of secondary structure topology, in particular, the β-sheet. Efficient NOESY cross-peak assignments were performed using CYANA version 1.05 with the CANDID protocol. Initially, 638 unambiguous NOEs were manually identified, and then the CANDID protocol provided approximately 500 restraints. Finally, the structure was calculated using CNS version 1.1, with 63 residual $^{1}D_{NH}$ dipolar couplings being added to the previously obtained distance and angle restraints.

Figure 5A depicts the backbone of the final 30 structures derived from the NMR data, showing that the atomic coordinates throughout the protein molecule have been well-defined except for the N- and C-terminal residues (residues 177−184 and 255, respectively). The average rms deviations calculated from the averaged structure were 0.16 and 0.52 Å for the backbone and all heavy atoms of the well-defined region (residues 185−254), respectively. The statistics of the structures are given in Table 1.

Structure of CwlCr. CwlCr adopts a βαββαβ-fold, comprising a layer consisting of an antiparallel β-sheet and two α-helices. The β-sheet is composed of β1 (residues 185−193), β2 (residues 214−218), β3 (residues 221−229), and β4 (residues 250−254) and is backed by α-helices α1 (residues 196−209) and α2 (residues 232−245) (Figures 1B and 5A,B). The main frame of the fold consists of a curled β-sheet, which resembles a horse saddle (Figure 5A,B).

The hydrogen bond network that defines the β-sheet topology is clearly identified by direct observation via $^{h3}J_{NC'}$

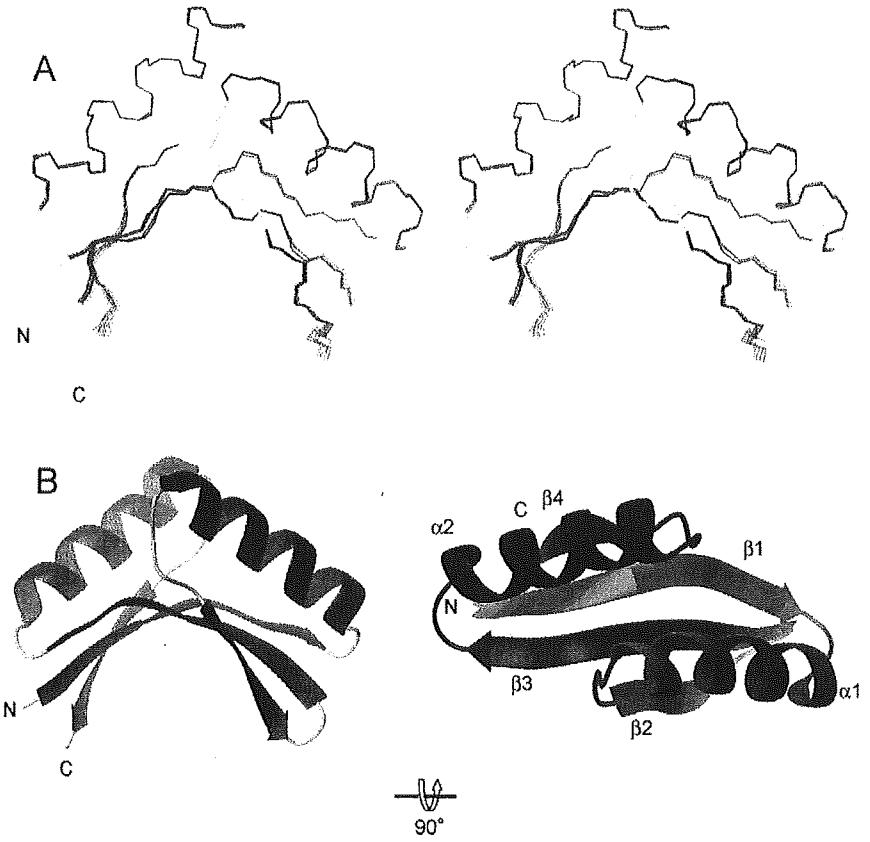

FIGURE 5: Solution structure of CwlCr. (A) Stereoview of the backbone superpositions of the final 30 simulated annealing structures of CwlCr. Helices and strands are colored red and blue, respectively. Residues 184−255 are shown. (B) Ribbon drawing of the representative structure of CwlCr in two different views. The molecular orientation in the left panel is the same as that in panel A, and the four-stranded β-sheet and α-helices are colored blue and red, respectively. The right panel shows a 90° rotation of the left panel about the horizontal axis. Repeat 1 and repeat 2 are colored green and blue, respectively.

couplings across the hydrogen bonds (Figure 4). The first strand, β1, forms a central part of the β-sheet with strand β3 in an antiparallel manner, and β4 and β2 contacted strands β1 and β3, respectively (Figures 4 and 5A,B). Additionally, $^{h3}J_{NC'}$ couplings show the presence of two β-bulges that are formed between strands β1 and β3 in the central part of the β-sheet. In the $^{h3}J_{NC'}$HNCO spectrum used for the detection of $^{h3}J_{NC'}$ couplings, a cross-peak was observed between the carbonyl group of G227 and the amide group of V188, while the amide group of I226 gave no detectable cross-peak. These observations indicated that a hydrogen bond is formed between G227 and V188, forming the β-bulge structure with a bend at the main chain position of G227 (Figure 4). Similarly, a cross-peak was observed between the carbonyl group of V191 and the amide group of V224, while the amide group of G190 gave no detectable cross-peak, indicating the presence of a hydrogen bond between V191 and V224, forming the β-bulge structure (Figure 4).

Interestingly, CwlCr is composed of two highly homologous repeat sequences that are 68% identical (Figure 1A). The first sequence repeat comprises (residues 184−219) strand β1, helix α2, and strand β2, while the second sequence repeat (residues 220−255) comprises strand β3, helix α2, and strand β4. Although CwlCr contains the two sequential sequence repeats, our structure determination revealed that the individual repeats do not form separate domains. Rather, the overall fold of the molecule is formed by numerous contacts between the two repeats (Figures 4 and Figure 5A,B). In addition to the aforementioned hydrogen bond network between the β-strands, the inward-facing residues on the β-sheet and α-helices form a hydrophobic core.

Conserved hydrophobic residues, noted as alignment positions *a*−*i* in Figure 1B, are likely to play key roles in the formation of the tertiary structure. Figure 6A shows the hydrophobic interactions within the protein core. I190 and I226 (position *c*) interact with each other, and are surrounded by V188 and V224 (position *b*) located at the center of the β-sheet (Figure 6A). L202 and L238 (position *f*) interact with F247 and F211 (position *h*), respectively, on the α-helices packing the core of the β-sheet (Figure 6A). A206 and A242 (position *g*) on the α-helices also form part of the core (Figure 6A).

Panels B and C of Figure 6 show the hydrophobic interactions on the edges of the protein. These stabilize the N-terminal tips of the α-helices on the β-sheet. A199 and A235 (position *e*) interact with V225 and V188 (position *b*), respectively, and also interact with V215 and V251 (position *i*), respectively, contributing to the interaction between the α-helices and the β-sheet. The aromatic rings of the conserved residues (positions *a* and *d*) interact with aliphatic β-methylene and the Hα atom. Y222 and Y186 (position *a*) interact with Hα atoms of K196 and K232, respectively. The Hα signals of these residues show significant upfield shifts (2.71 and 2.77 ppm, respectively) due to ring current effects. These observations confirm the interaction between the aromatic rings and the Hα atoms of the

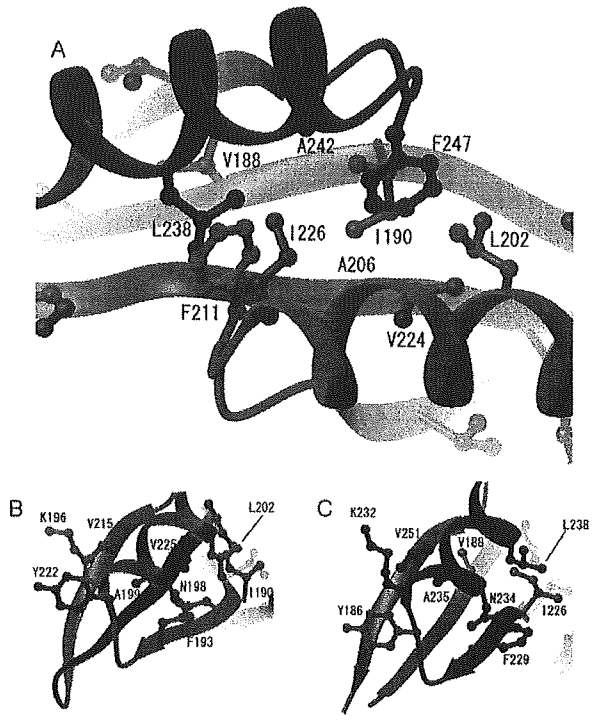

FIGURE 6: Hydrophobic interactions mediated by conserved residues. (A) Ribbon representation with a ball-and-stick model of the side chains at the protein core. (B and C) Hydrophobic interaction at the edges of the protein.

lysine residues. F193 and F229 (position *d*) interact with the β-methylenes of N198 and N234, respectively. The ^{1}H signals of these β-methylenes are well separated, implying rigidity of the side chain, and show upfield shifts due to ring current effects (chemical shifts of the upfield component of their signals are 1.93 and 1.98 ppm, respectively). This confirmed the interaction between the aromatic rings and the β-methylenes of the asparagines.

The residues (positions $a-i$) are completely conserved between repeat 1 and repeat 2 of CwlCr. They are located symmetrically within the structure, and are conserved throughout the sporulation repeat family according to the Pfam database (*16*), suggesting the existence of a common folding pattern composed of the two repeats similar to the CwlCr structure with numerous contacts between the two repeats. It should be noted that the sporulation repeats exist as two or more tandem repeats in most of the proteins that possess them. This supports the notion of a common fold consisting of two tandem repeat sequences. In fact, the C-terminal domain of FtsN consists of two tandem sporulation repeats folded into a similar structure showing a high *Z* score, 5.6, according to a DALI database search. The rms deviation between CwlCr and the C-terminal domain of FtsN (*40*) (PDB entry 1UTA) is 1.88 Å over 34 Cα coordinates for residues in the regions represented by secondary structure elements (CwlCr residues 187−192, 200−208, 212−215, 223−226, 238−245, and 250−252).

Circularly Permuted Repeat Mutant. Assuming that the core-forming conserved hydrophobic residues ($a-f$) are key determinants of the structural integrity, a circularly permuted repeat mutant may form a similar tertiary structure. In an effort to investigate this notion, we constructed a circularly permuted repeat mutant, termed CwlCr21(1−72) (Figure 1A). Recombinant CwlCr21 was expressed as a hexahistidine-tagged peptide in *E. coli* and subsequently purified by standard methods. No significant degradation had occurred during the purification process, and a relatively large amount of the recombinant protein was obtained (approximately 20 mg of ^{13}C- and ^{15}N-labeled CwlCr21/L of M9 culture). This was in contrast to the expression and purification of each single repeat being associated with a low yield due to degradation (data not shown). These results implied that CwlCr21 would also form a stable structure by the two repeats.

Furthermore, the ^{1}H−^{15}N HSQC spectrum of CwlCr21 shows well-dispersed and relatively sharp signals, indicating that CwlCr21 adopts a well-packed structure (Figure 7A). The main chain resonance assignments were obtained from HNCACB, HN(CO)CACB, HN(CA)CO, and HNCO experiments, and confirmed by HN(CO-TOCSY)NH experiments. The chemical shift index (*41*) of Cα and the chemical shift deviations of Cα and Cβ (represented as δCα − δCβ) (*42*) indicate that the secondary structure of CwlCr21 consists of $\beta\alpha\beta\beta\alpha\beta$, which is almost identical to that of CwlCr (Figure 7A). Additionally, the $^{h3}J_{NC'}$HNCO experiment shows the presence of hydrogen bonds between the β-strands (Figure 4). The observed hydrogen bonds indicate that strands $\beta1-\beta4$ form a single antiparallel β-sheet layer. Although the observed hydrogen bonds can only partially be determined given the quality of the spectrum, enough information has been gleaned to determine that this β-sheet topology is identical to that of CwlCr. (The strips of the $^{h3}J_{NC'}$HNCO spectra recorded on CwlCr and CwlCr21 are shown in Figures S1 and S2 of the Supporting Information.)

These data imply that the tertiary structure of CwlCr21 is similar to that of CwlCr. Therefore, the repeat sequences are exchangeable, which confirms that the conserved core-forming residues are key determinants of protein folding. This reinforces the notion of a common folding pattern formed by two sporulation-related repeats.

Domain-Swapped Dimer? The CwlCr21 data indicate that the repeat sequences of CwlCr are exchangeable. This result raises another concern that CwlCr forms a domain-swapped dimer. Nevertheless, fine agreement exists between the observed residual dipolar couplings and the determined structure (Table 1), indicating that almost all of CwlCr exists as a monomer in solution under normal conditions. Furthermore, analytical gel-filtration chromatography using Superdex-75 linked to an AKTA Purifier system (Amasharm Biosciences) showed that CwlCr exits as a monomer, with no peaks corresponding to dimer (or higher multimer) molecular weights being detected (data not shown). Thus, we conclude that CwlCr exists as a monomer under normal conditions.

To date, several domain-swapped dimers have been reported (*43*−*45*). The domain-swapped dimers are in a meta-stable, kinetically trapped state at room temperature. Thus, in formation of a domain-swapped dimer, it is necessary to ensure transient destabilizing conditions such as low pH, and the presence of organic solvents or chaotropic agents at high protein concentrations (*43*, *45*). These destabilizing conditions were not tested in this study. The generation of a CwlCr domain-swapped dimer remains an interesting objective from a protein engineering viewpoint.

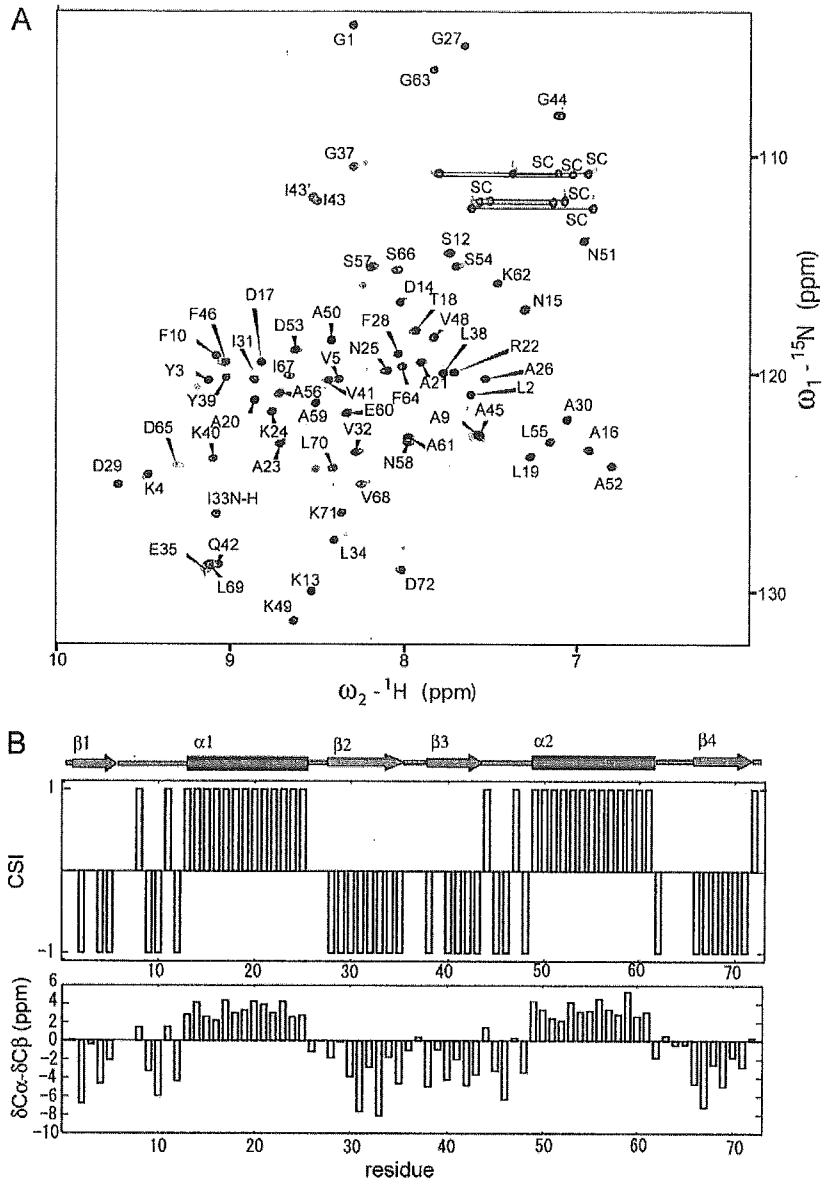

FIGURE 7: (A) ^{15}N−^{1}H HSQC spectrum of CwlCr21. The spectrum was obtained with 0.8 mM CwlCr21 at pH 6.5 and 30 °C on a Bruker DRX 800. The SC label indicates side chain peaks of asparagine or glutamine residues. (B) Secondary structure of CwlCr21. The top panel shows the score of the chemical shift index of the Cα atom. Estimated secondary structure is shown at the top of the panel. The bottom panel shows chemical shift deviations of Cα and Cβ atoms. Deviations from the random values of Cα and Cβ are shown as $\delta C\alpha - \delta C\beta$.

Peptidoglycan Binding. Titration experiments were employed using ^{1}H−^{15}N HSQC spectra in an effort to establish the peptidoglycan interaction surfaces of CwlCr. However, since peptidoglycan obtained from *B. subtilis* was insoluble in aqueous solution, NMR experiments could not be applied in a straightforward manner.

Thus, we initially tried to monitor the interactions between CwlCr and the building blocks of the peptidoglycan, (1) diaminopimelic acid, (2) Ala-D-γ-Glu-Lys-D-Ala-D-Ala, (3) GlcNAc, and (4) GlcNAcMurNAcAlaGln, since these molecules could be readily dissolved in aqueous solution. We expected to obtain some clues pertaining to the binding sites, even if the binding was predicted to be rather weak compared to that expected for intact peptidoglycan. However, addition of a large excess of these molecules to CwlCr showed no signal perturbations, suggesting that these building blocks in and of themselves were insufficient for CwlCr binding, or that the binding was too weak to be detected by NMR (data not shown).

We next improved the solubility of the peptidoglycan by enzymatic digestion with intact CwlC. The digested short peptidogylcan fragment was soluble up to 0.5 mg/mL. Figure 8A shows the signal perturbation following the addition of digested products. To identify the peptidoglycan binding regions of CwlCr, significantly affected residues were mapped on the structure of CwlCr. The residues are essentially confined to two regions, the N-terminal tip of the two α-helices and the β-sheet regions near these on the edges of the protein (sites 1 and 2) (Figure 8B). The exposed residues are K194, V195, K196, A197, N198, D200, and S201 in site 1 and S230, S231, K232, D233, N234, D236, and T237 in site 2. In particular, N198 and N234, which are

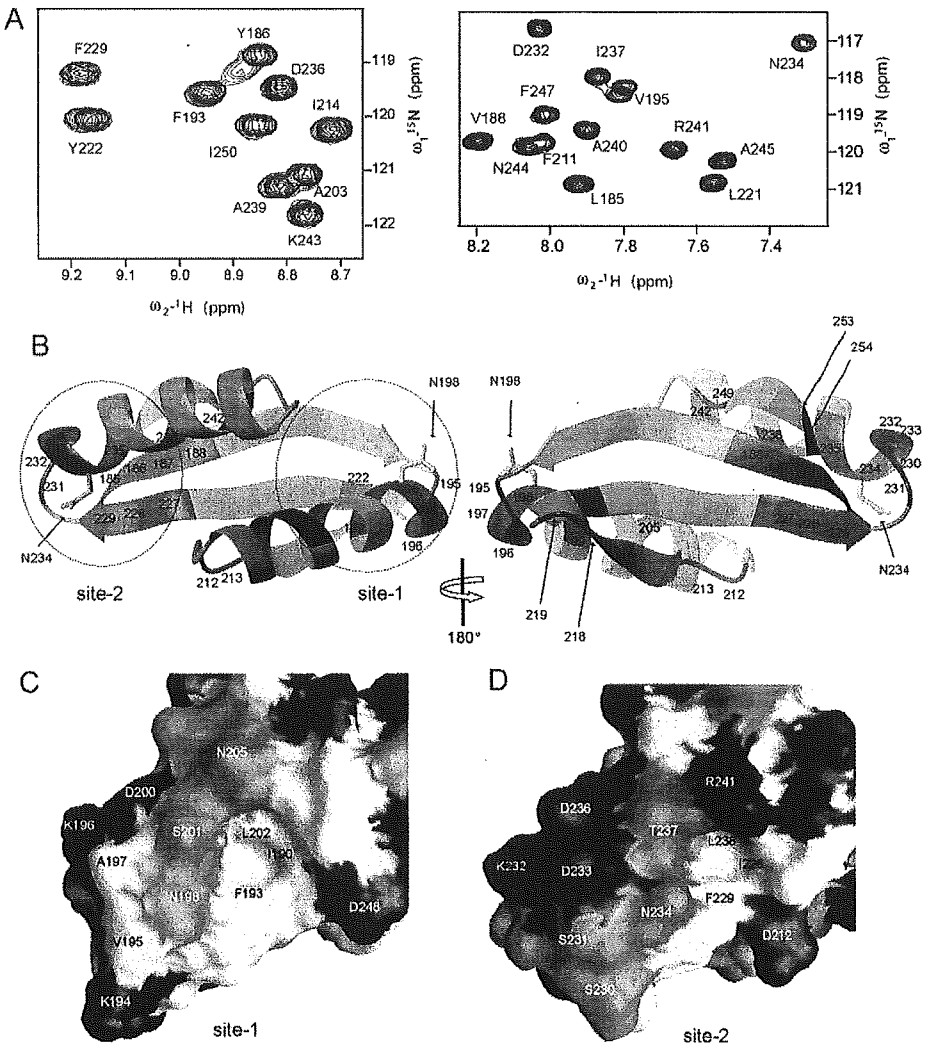

FIGURE 8: Chemical shift perturbation experiments. (A) Selected region of the $^{15}N-^{1}H$ HSQC spectra of CwlCr, recorded in the absence (black) or presence (red) of 0.5 mg/mL digested peptidoglycan. The threshold of the perturbed spectrum is set to 20-fold lower than that of the control for clarity. (B) Representation of the ribbon model with color coding to show the effect following the addition of 0.5 mg/mL digested peptidoglycan. Residues that show weighted average shift difference values, $\delta_{ave}/\delta_{max}$, larger than 0.25 are colored pink with the residue number ($\delta_{max} = 0.046$ ppm). Residues whose signal intensity $[(I_{ref} - I_{per})/I_{ref}]$ is reduced to >96% of the original values are colored red with the residue number. Residues whose value of both weighted average shift difference and intensity reduction are larger than the threshold are also colored red. Side chains of Asn198 and Asn234 are shown as orange sticks. Patches with confined perturbed residues are circled. (C and D) The molecular surfaces of sites 1 and 2 of CwlCr are shown. The molecular orientations in panels C and D are the same as in panels B and C of Figure 6, respectively. The figures were prepared using GRASP (*56*).

exposed on the surface at the center of the two perturbed sites, represent conserved invariant residues as found with other cell wall lytic enzymes (Figures 1B and 8C,D).

Mutation analyses showed that the N198D and N234D double mutation completely impaired peptidoglycan binding, while each single mutant retained ~75% binding activity, indicating that these two residues participate in peptidoglycan binding. Extensive site-directed mutagenesis and the significance of the findings to binding activity will be published elsewhere (T. Shida et al., manuscript in preparation). N198 and N234 residues are exposed on the edges of the domain, the equivalent positions on the symmetrical structure, and are located approximately 28 Å from each other (Figure 8B). The local environments around N198 and N234 are also equivalent, and involve contact with the conserved aromatic ring of phenylalanines, F193 and F229, respectively (position *d*) (Figure 6B,C). These observations suggest that CwlCr possesses two equivalent symmetrically located binding sites. The chemical shift perturbations of site 2 were more affected than those of site 1, but this may not necessarily reflect a difference in the peptidoglycan binding preference of the two sites. Although both site 1 and site 2 are composed of the tip of the α-helix and β-sheet, the β-sheet of site 2 includes the N-terminal and C-terminal region, in contrast to that of site 1 which includes the β-hairpin (Figures 6B and 8B). Thus, NMR signals of site 2 are likely to be more susceptible to peptidoglycan binding.

Surface properties of sites 1 and 2 are shown in Figure 8C,D. In both sites, concave hydrophobic patches exist near the key asparagine residues, N198 and N234. Portions of the side chains of I190, F193, and L202 form the patch in site 1, and those of I226, F229, and L238 form the patch in site 2 (Figure 8C,D). These hydrophobic residues are highly conserved. This suggests the conserved hydrophobic surfaces

adjacent to the polar side chains of the asparagines are important for CwlCr−peptidoglycan interaction. In contrast, functional groups of the side chains of K194, V195, and A197 in site 1 and S230, S231, and D233 in site 2, which are located at the turns connecting β1 and α1, and β3 and α2, and are located at tips of the helices, are not conserved between the two sites (Figure 8C,D) or among other cell wall lytic enzymes, implying these residues are not important for peptidoglycan binding. Chemical shift perturbations of these residues are likely to reflect conformational changes of the turns caused by binding of peptidoglycan to the flanking polar−hydrophobic regions but not direct binding.

The peptidoglycan layer consists of a carbohydrate backbone of alternating units of *N*-acetylglucosamine and *N*-acetylmuramic acid. The *N*-acetylmuramic acid residues are cross-linked with the oligopeptide linker, including a branch formed by diaminopimelic acid (*46*, *47*). The layers stacked, and carbohydrate backbones and oligopeptide linkers form lattice-like three-dimensional structures. Thus, bivalent binding exerted by two equivalent symmetrical binding sites on pseudo-2-fold symmetric structure may be advantageous, since it increases the affinity for peptidoglycan consisting of quasi-periodic structures.

By analogy, it was reported that Cyanovirin-N binds N-linked high-mannose oligosaccharides on gp120 through two major sugar binding sites (*48*). Besides, in the case of lectin−oligosaccharide binding, many naturally occurring oligosaccharides and glycoconjugates are reported to be multivalent, thereby increasing the apparent affinity for lectins relative to monovalent analogues, implying that multivalent binding is advantageous (*49*).

Some tertiary structures typical of a "peptidoglycan binding domain as a protein module" have been reported, including the LysM domain (*50*) and PGRPs (*51*−*53*). In the case of LysM and PGRP, however, multivalent binding was not reported. The difference in the binding mode may reflect the difference in their tertiary structure. That is, CwlCr and Cyanovirin-N adopt a 2-fold symmetric structure, unlike LysM and PGRP.

Obviously, further quantitative biochemical analyses of CwlCr and peptidoglycan interactions, such as the number of binding sites and stoichiometry, are required. At present, more detailed analyses have been hampered by difficulties in handling peptidoglycan. Access to and use of a new variety of chemically synthetic peptidoglycan building blocks may allow us to overcome the inherent problems associated with the use of peptidoglycan.

Conclusion. We have determined the tertiary structure of the sporulation-related repeats in CwlC amidase, CwlCr. Because of the characteristic repeat sequences, the ^{1}H and ^{13}C resonances heavily overlapped, and thus, advanced NMR techniques were required to determine the structure, such as 3D (H)N(CO-TOCSY)-NH for the assignments, $^{h3}J_{NC'}$HNCO for the hydrogen bond constraints, and ^{1}H−^{15}N IPAP for the residual $^{1}D_{NH}$ couplings. The repeat sequence adopts a remarkable 2-fold symmetric structure, consisting of a $\beta\alpha\beta\beta\alpha\beta$-fold. The repeats of CwlCr exhibit interesting behavior in that the repeats can be swapped, and the circularly permuted variant forms a similar tertiary structure, indicating that the conserved hydrophobic residues are keys for folding of the repeats. Chemical shift perturbation experiments indicate that CwlCr directly binds to peptidoglycan, and at least two interaction sites on the edges of the protein have been identified.

ACKNOWLEDGMENT

We thank Dr. Markus Zweckstetter for cordial instructions for PALES and Dr. Hidenori Kato for help in the sample preparation. We are grateful to Junko Tsukamoto for her assistance with the mass spectroscopy.

SUPPORTING INFORMATION AVAILABLE

Strip plot of the 3D $^{h3}J_{NC'}$ spectrum of CwlCr (Figure S1) and CwlCr21 (Figure S2). This material is available free of charge via the Internet at http://pubs.acs.org.

REFERENCES

1. Rogers, H. J., Perkins, H. R., and Ward, J. B. (1980) *Microbial cell walls and membranes*, Chapman and Hall, London.
2. Doyle, R. J., and Koch, A. L. (1987) The functions of autolysins in the growth and division of *Bacillus subtilis*, *Crit. Rev. Microbiol. 15*, 169−222.
3. Stockman, G. D., and Holtje, J.-V. (1994) Microbial peptidoglycan (murein) hydrolases, *Bacterial cell wall*, Elsevier, Amsterdam.
4. Ayusawa, D., Yoneda, Y., Yamane, K., and Maruo, B. (1975) Pleiotropic phenomena in autolytic enzyme(s) content, flagellation, and simultaneous hyperproduction of extracellular α-amylase and protease in a *Bacillus subtilis* mutant, *J. Bacteriol. 124*, 459−469.
5. Fein, J. E. (1979) Possible involvement of bacterial autolytic enzymes in flagellar morphogenesis, *J. Bacteriol. 137*, 933−946.
6. Harz, H., Burgdorf, K., and Holtje, J. V. (1990) Isolation and separation of the glycan strands from murein of *Escherichia coli* by reversed-phase high-performance liquid chromatography, *Anal. Biochem. 190*, 120−128.
7. Herbold, D. R., and Glaser, L. (1975) *Bacillus subtilis N*-acetylmuramic acid L-alanine amidase, *J. Biol. Chem. 250*, 1676−1682.
8. Kuroda, A., and Sekiguchi, J. (1991) Molecular cloning and sequencing of a major *Bacillus subtilis* autolysin gene, *J. Bacteriol. 173*, 7304−7312.
9. Lazarevic, V., Margot, P., Soldo, B., and Karamata, D. (1992) Sequencing and analysis of the *Bacillus subtilis* lytRABC divergon: A regulatory unit encompassing the structural genes of the *N*-acetylmuramoyl-L-alanine amidase and its modifier, *J. Gen. Microbiol. 138*, 1949−1961.
10. Margot, P., Mauel, C., and Karamata, D. (1994) The gene of the *N*-acetylglucosaminidase, a *Bacillus subtilis* 168 cell wall hydrolase not involved in vegetative cell autolysis, *Mol. Microbiol. 12*, 535−545.
11. Rashid, M. H., Mori, M., and Sekiguchi, J. (1995) Glucosaminidase of *Bacillus subtilis*: Cloning, regulation, primary structure and biochemical characterization, *Microbiology 141*, 2391−2404.
12. Rogers, H. J., Taylor, C., Rayter, S., and Ward, J. B. (1984) Purification and properties of autolytic endo-β-*N*-acetylglucosaminidase and the *N*-acetylmuramyl-L-alanine amidase from *Bacillus subtilis* strain 168, *J. Gen. Microbiol. 130*, 2395−2402.
13. Smith, T. J., and Foster, S. J. (1995) Characterization of the involvement of two compensatory autolysins in mother cell lysis during sporulation of *Bacillus subtilis* 168, *J. Bacteriol. 177*, 3855−3862.
14. Kuroda, A., Sugimoto, Y., Funahashi, T., and Sekiguchi, J. (1992) Genetic structure, isolation and characterization of a *Bacillus licheniformis* cell wall hydrolase, *Mol. Gen. Genet. 234*, 129−137.
15. Shida, T., Hattori, H., Ise, F., and Sekiguchi, J. (2001) Mutational analysis of catalytic sites of the cell wall lytic *N*-acetylmuramoyl-L-alanine amidases CwlC and CwlV, *J. Biol. Chem. 276*, 28140−28146.
16. Bateman, A., Coin, L., Durbin, R., Finn, R. D., Hollich, V., Griffiths-Jones, S., Khanna, A., Marshall, M., Moxon, S., Sonnhammer, E. L., Studholme, D. J., Yeats, C., and Eddy, S. R. (2004) The Pfam protein families database, *Nucleic Acids Res. 32*, 138−141.

17. Ruckert, M., and Otting, G. (2000) Alignment of biological macromolecules in novel nonionic liquid crystalline media for NMR experiments, *J. Am. Chem. Soc. 122*, 7793−7797.
18. Muhandiram, D. R., and Kay, L. E. (1994) Gradient-Enhanced Triple-Resonance Three-Dimensional NMR Experiments with Improved Sensitivity, *J. Magn. Reson., Ser. B 103*, 203−216.
19. Kay, L. E., Xu, G. Y., and Yamazaki, T. (1994) Enhanced-Sensitivity Triple-Resonance Spectroscopy with Minimal H_2O Saturation, *J. Magn. Reson., Ser. A 129*, 129−133.
20. Delaglio, F., Grzesiek, S., Vuister, G. W., Zhu, G., Pfeifer, J., and Bax, A. (1995) NMRPipe: A multidimensional spectral processing system based on UNIX pipes, *J. Biomol. NMR 6*, 277−279.
21. Goddard, T. D., and Kneller, D. G. (1999) *SPARKY3*, University of California, San Francisco.
22. Cavanagh, J., Fairbrother, W. J., Palmer, A. G., III, and Skelton, N. J. (1996) *Protein NMR Spectroscopy*, Acdemic Press, San Diego.
23. Sattler, M. S., Schleucher, J., and Griesinger, C. (1999) Heteronuclear multidimensional NMR experiments for the structure determination of proteins in solution employing pulsed field gradients, *Prog. Nucl. Magn. Reson. Spectrosc. 34*, 93−158.
24. Clowes, R. T., Boucher, W., Hardman, C. H., Domaille, P. J., and Laue, E. D. (1993) A 4D HCC(CO)NNH experiment for the correlation of aliphatic side-chain and backbone resonances in ^{13}C/^{15}N-labeled proteins, *J. Biomol. NMR 3*, 349−354.
25. Liu, A., Riek, R., Wider, G., von Schroetter, C., Zahn, R., and Wüthrich, K. (2000) NMR experiments for resonance assignments of ^{13}C, ^{15}N doubly-labeled flexible polypeptides: Application to the human prion protein hPrP(23−230), *J. Biomol. NMR 16*, 127−138.
26. Neri, D., Szyperski, T., Otting, G., Senn, H., and Wüthrich, K. (1989) Stereospecific nuclear magnetic resonance assignments of the methyl groups of valine and leucine in the DNA-binding domain of the 434 repressor by biosynthetically directed fractional ^{13}C labeling, *Biochemistry 28*, 7510−7516.
27. Cordier, F., and Grzesiek, S (1999) Direct Observation of Hydrogen Bonds in Proteins by Interresidue $^{3h}J_{NC'}$ Scalar Couplings, *J. Am. Chem. Soc. 121*, 1601−1602.
28. Cornilescu, G., Hu, J. S., and Bax, A. (1999) Identification of the Hydrogen Bonding Network in a Protein by Scalar Couplings, *J. Am. Chem. Soc. 121*, 2949−2950.
29. Cornilescu, G., Delaglio, F., and Bax, A. (1999) Protein backbone angle restraints from searching a database for chemical shift and sequence homology, *J. Biomol. NMR 13*, 289−302.
30. Archer, S. J., Ikura, M., Torchia, D. A., and Bax, A. (1991) An alternative 3D NMR technique for correlating backbone ^{15}N with side-chain Hβ resonances in larger proteins, *J. Magn. Reson. 95*, 636−641.
31. Grzesiek, S., Ikura, M., Clore, G. M., Gronenborn, A. M., and Bax, A. (1992) A 3D triple-resonance NMR technique for qualitative measurement of carbonyl-Hβ J couplings in isotopically enriched protein, *J. Magn. Reson. 96*, 215−221.
32. Ottiger, M., Delaglio, F., and Bax, A. (1998) Measurement of J and Dipolar Couplings from Simplified Two-Dimensional NMR Spectra, *J. Magn. Reson. 131*, 373−378.
33. Herrmann, T., Guntert, P., and Wüthrich, K. (2002) Protein NMR structure determination with automated NOE assignment using the new software CANDID and the torsion angle dynamics algorithm DYANA, *J. Mol. Biol. 319*, 209−227.
34. Brunger, A. T., Adams, P. D., Clore, G. M., DeLano, W. L., Gros, P., Grosse-Kunstleve, R. W., Jiang, J. S., Kuszewski, J., Nilges, M., Pannu, N. S., Read, R. J., Rice, L. M., Simonson, T., and Warren, G. L. (1998) Crystallography & NMR system: A new software suite for macromolecular structure determination, *Acta Crystallogr. D54*, 905−921.
35. Zweckstetter, M., and Bax, A. (2000) Prediction of Sterically Induced Alignment in a Dilute Liquid Crystalline Phase: Aid to Protein Structure Determination by NMR, *J. Am. Chem. Soc. 122*, 3791−3792.
36. Laskowski, R. A., Rullmannn, J. A., MacArthur, M. W., Kaptein, R., and Thornton, J. M. (1996) AQUA and PROCHECK-NMR: Programs for checking the quality of protein structures solved by NMR, *J. Biomol. NMR 8*, 477−486.
37. Koradi, R., Billete, M., and Wuthrich, K. (1996) MOLMOL: A program for display and analysis of macromolecular structures, *J. Mol. Graphics 14*, 51−55.
38. Garrett, D. S., Seok, Y. J., Peterkofsky, A., Clore, G. M., and Gronenborn, A. M. (1997) Identification by NMR of the binding surface for the histidine-containing phosphocarrier protein HPr on the N-terminal domain of enzyme I of the *Escherichia coli* phosphotransferase system, *Biochemistry 36*, 4393−4398.
39. Foster, M. P., Wuttke, D. S., Clemens, K. R., Jahnke, W., Radhakrishnan, I., Tennant, L., Reymond, M., Chung, J., and Wright, P. E. (1988) Chemical shift as a probe of molecular interfaces: NMR studies of DNA binding by the three amino-terminal zinc finger domains from transcription factor IIIA, *J. Biomol. NMR 12*, 51−71.
40. Yang, J. C., Van Den Ent, F., Neuhaus, D., Brevier, J., and Lowe, J. (2004) Solution structure and domain architecture of the divisome protein FtsN, *Mol. Microbiol. 52*, 651−660.
41. Wishart, D. S., and Sykes, B. D. (1994) Chemical shifts as a tool for structure determination, *Methods Enzymol. 239*, 363−392.
42. Spera, S., and Bax, A. (1991) Empirical correlation between protein backbone conformation and Cα and Cβ ^{13}C nuclear magnetic resonance chemical shifts, *J. Am. Chem. Soc. 113*, 5490−5492.
43. Bennett, M. J., Choe, S., and Eisenberg, D. (1994) Domain swapping: Entangling alliances between proteins, *Proc. Natl. Acad. Sci. U.S.A. 91*, 3127−3131.
44. Liu, Y., Hart, P. J., Schlunegger, M. P., and Eisenberg, D. (1998) The crystal structure of a 3D domain-swapped dimer of RNase A at a 2.1-Å resolution, *Proc. Natl. Acad. Sci. U.S.A. 95*, 3437−3442.
45. Barrientos, L. G., Louis, J. M., Botos, I., Mori, T., Han, Z., O'Keefe, B. R., Boyd, M. R., Wlodawer, A., and Gronenborn, A. M. (2002) The domain-swapped dimer of cyanovirin-N is in a metastable folded state: Reconciliation of X-ray and NMR structures, *Structure 10*, 673−686.
46. Atrih, A., Zollner, P., Allmaier, G., and Foster, S. J. (1996) Structural analysis of *Bacillus subtilis* 168 endospore peptidoglycan and its role during differentiation, *J. Bacteriol. 178*, 6173−6183.
47. Atrih, A., Bacher, G., Allmaier, G., Williamson, M. P., and Foster, S. J. (1999) Analysis of peptidoglycan structure from vegetative cells of *Bacillus subtilis* 168 and role of PBP 5 in peptidoglycan maturation, *J. Bacteriol. 181*, 3956−3966.
48. Shenoy, S. R., Barrientos, L. G., Ratner, D. M., O'Keefe, B. R., Seeberger, P. H., Gronenborn, A. M., and Boyd, M. R. (2002) Multisite and multivalent binding between cyanovirin-N and branched oligomannosides: Calorimetric and NMR characterization, *Chem. Biol. 9*, 1109−1118.
49. Dam, T. K., Roy, R., Das, S. K., Oscarson, S., and Brewer, C. F. (2002) Binding of multivalent carbohydrates to concanavalin A and *Dioclea grandiflora* lectin. Thermodynamic analysis of the "multivalency effect", *J. Biol. Chem. 275*, 14223−14230.
50. Bateman, A., and Bycroft, M. (2000) The structure of a LysM domain from *E. coli* membrane-bound lytic murein transglycosylase D (MltD), *J. Mol. Biol. 299*, 1113−1119.
51. Liepinsh, E., Genereux, C., Dehareng, D., Joris, B., and Otting, G. (2003) NMR structure of *Citrobacter freundii* AmpD, comparison with bacteriophage T7 lysozyme and homology with PGRP domains, *J. Mol. Biol. 327*, 833−842.
52. Kim, M. S., Byun, M., and Oh, B. H. (2003) Crystal structure of peptidoglycan recognition protein LB from *Drosophila melanogaster*, *Nat. Immunol. 4*, 787−793.
53. Reiser, J. B., Teyton, L., and Wilson, I. A. (2004) Crystal structure of the *Drosophila* peptidoglycan recognition protein (PGRP)-SA at 1.56 Å resolution, *J. Mol. Biol. 340*, 909−917.
54. Thompson, J. D., Higgins, D. G., and Gibson, T. J. (1994) CLUSTAL W: Improving the sensitivity of progressive multiple sequence alignment through sequence weighting, position-specific gap penalties and weight matrix choice, *Nucleic Acids Res. 22*, 4673−4680.
55. Clamp, M., Cuff, J., Searle, S. M., and Barton, G. J. (2004) The Jalview Java alignment editor, *Bioinformatics 20*, 426−427.
56. Nicholls, A., Sharp, K. A., and Honig, B. (1991) Protein folding and association: Insights from the interfacial and thermodynamic properties of hydrocarbons, *Proteins: Struct., Funct., Genet. 11*, 281−296.

BI050624N

Amino Acid Residues Involved in Substrate Recognition of the *Escherichia coli* Orf135 Protein†

Emiko Iida,‡ Kazuya Satou,‡ Masaki Mishima,§ Chojiro Kojima,§ Hideyoshi Harashima,‡ and Hiroyuki Kamiya*,‡

Graduate School of Pharmaceutical Sciences, Hokkaido University, Kita-12, Nishi-6, Kita-ku, Sapporo 060-0812, Japan, and Graduate School of Biological Sciences, Nara Institute of Science and Technology, 8916-5 Takayama, Ikoma, Nara 630-0101, Japan

Received September 8, 2004; Revised Manuscript Received February 8, 2005

ABSTRACT: The *Escherichia coli* Orf135 protein, a MutT-type enzyme, hydrolyzes mutagenic 2-hydroxy-dATP (2-OH-dATP) and 8-hydroxy-dGTP, in addition to dCTP and 5-methyl-dCTP, and its deficiency causes increases in both the spontaneous and H_2O_2-induced mutation frequencies. To identify the amino acid residues that interact with these nucleotides, the Glu-33, Arg-72, Arg-77, and Asp-118 residues of Orf135, which are candidates for residues interacting with the base, were substituted, and the enzymatic activities of these mutant proteins were examined. The mutant proteins with a substitution at the 33rd, 72nd, and 118th amino acid residues displayed activities affected to various degrees for each substrate, suggesting the involvement of these residues in substrate binding. On the other hand, the mutant protein with a substitution at the 77th Arg residue had activitiy similar to that of the wild-type protein, excluding the possibility that this Arg side chain is involved in base recognition. In addition, the expression of some Orf135 mutants in *orf135*$^-$ *E. coli* reduced the level of formation of *rpoB* mutants elicited by H_2O_2. These results reveal the residues involved in the substrate binding of the *E. coli* Orf135 protein.

Organisms are equipped with mechanisms to prevent mutations caused by the incorporation of oxidized deoxyribonucleotides (*1*, *2*). The *Escherichia coli* MutT and its mammalian counterpart (MTH1) proteins hydrolyze 8-OH-dGTP[1] to the monophosphate derivative (*3*, *4*). Deficiencies in these proteins result in increased mutation frequency and enhanced tumor formation (*5*, *6*). Thus, these types of enzymes are quite important for nucleotide pool sanitization.

The *E. coli* Orf135 protein, another MutT-type enzyme, hydrolyzes 2-OH-dATP and 8-OH-dGTP, in addition to 5-Me-dCTP and dCTP (*7*, *8*). Its deficiency causes increases in both the spontaneous and H_2O_2-induced mutation frequencies (*9*). The 2-OH-dATP hydrolyzing activity of Orf135 may be a crucial mechanism for preventing mutations induced by this damaged DNA precursor, because 2-OH-dATP is mutagenic in *E. coli* and mutations are induced more frequently in an *orf135*$^-$ strain than in the isogenic *orf135*$^+$ strain (*9*, *10*). The importance of 2-OH-dATP is also supported by the observation that the expression of MTH1 harboring the D119A mutation, which is unable to hydrolyze 2-OH-dATP, only partially suppresses the cell dysfunction and delayed cell death of MTH1-null mouse embryo fibroblast cells, while the expression of wt MTH1 effectively suppresses these phenomena (*11*).

The overall structures of the *E. coli* MutT and mammalian MTH1 proteins, which both hydrolyze 8-OH-dGTP, resemble each other, although the level of sequence identity between the MTH1 and MutT proteins outside of the "phosphohydrolase module" or "MutT signature" is low (*12*). A model structure of the Orf135 protein was recently built, using the coordinates of the MutT protein as a template, and a nucleotide binding pocket was proposed by comparison with the structure of the human MTH1 protein and NMR titration experiments (see the Supporting Information). This model suggests that the Glu-33, Arg-72, Arg-77, and Asp-118 residues of Orf135 are exposed on the surface of the base-binding pocket, and thus are possible candidates for residues interacting with the base moieties of substrates.

In this study, to clarify the significance of these Orf135 amino acid residues in nucleotide binding, we carried out a site-directed mutagenesis study. The in vitro activities of the mutant proteins were examined by their abilities to hydrolyze 2-OH-dATP and 8-OH-dGTP, as well as 5-Me-dCTP and dCTP. Their in vivo activities were studied by determining whether the expression of the mutant proteins restored the mutator phenotype observed for the *orf135*$^-$ strain. The results obtained in this study revealed amino acid residues involved in the nucleotide binding of the *E. coli* Orf135 protein.

EXPERIMENTAL PROCEDURES

Materials. E. coli strain JD22899, an *orf135*$^-$ strain [*lacI*^{q}, *lacZ*ΔM15-*gal*$^-$, *F*$^-$, *orf135*::mini Tn10 (*kan*)] (T. Miki et

† This work was supported in part by Grants-in-Aid and 21st Century COE Research from the Ministry of Education, Culture, Sports, Science and Technology of Japan.

* To whom correspondence should be addressed. Telephone: +81-11-706-3733. Fax: +81-11-706-4879. E-mail: hirokam@pharm.hokudai.ac.jp.

‡ Hokkaido University.

§ Nara Institute of Science and Technology.

[1] Abbreviations: ROS, reactive oxygen species; 8-OH-dGTP, 8-hydroxy-2′-deoxyguanosine 5′-triphosphate; 8-OH-dGDP, 8-hydroxy-2′-deoxyguanosine 5′-diphosphate; 2-OH-dATP, 2-hydroxy-2′-deoxyadenosine 5′-triphosphate; 5-Me-dCTP, 5-methyl-2′-deoxycytidine 5′-triphosphate; wt, wild-type; GST, glutathione *S*-transferase; PCR, polymerase chain reaction; LB, Luria−Bertani; IPTG, isopropyl β-D-thiogalactopyranoside; amp, ampicillin.

10.1021/bi048071o CCC: $30.25
Published on Web 03/25/2005

Table 1: PCR Primers for Orf135 Mutants[a]

primer	sequence (5′ → 3′)[b]
E33A (+)	GATTATGGGCGTTTGCCGG
E33Q (+)	GGATTATGGCAGTTTGCCGG
E33D (+)	GATTATGGGACTTTGCCGGT
R72A (+)	AGCCATCAGGGCAGAAGTTTC
R72K (+)	AGCCATCAGAAAGAAGTTTCG
R77A (+)	TTTCGGGGGCGATTATCCAT
D118A (+)	CCCTGCTGCCATTCCATTAT
D118E (+)	CCCTGCTGAGATTCCATTATT
D118N (+)	GCCCCTGCTAACATTCCATT

[a] Primers corresponding to the sense strand are shown. Their complementary oligodeoxyribonucleotides were also used in the mutagenic PCR. [b] The targeted codons are underlined. The mutated positions are shown in bold.

al., unpublished results), was kindly provided by Y. Yamamoto and T. Miki. dATP, dGTP, dCTP, and pGEX-6P-3 DNA, containing the GST gene, were from Amersham Biosciences (Piscataway, NJ). 5-Me-dCTP was from F. Hoffmann-La Roche (Basel, Switzerland) and was purified by high-performance liquid chromatography. Oligodeoxyribonucleotides were purchased from Sigma Genosys Japan (Ishikari, Japan) in purified forms.

Preparation of Damaged Nucleotides. 8-OH-dGTP and 2-OH-dATP were prepared as previously described (*13*, *14*). These purified nucleotides were eluted as a single peak in both reverse-phase and anion-exchange HPLC (data not shown). They were stable under the assay conditions in the absence of Orf135 (data not shown).

Mutant Plasmid Construction. Mutant *orf135* genes were prepared by site-directed PCR mutagenesis using the wt *orf135* plasmid (*7*) as the template, mutagenic primers (Table 1), and high-fidelity Pyrobest DNA polymerase (Takara, Otsu, Japan). The mutant *orf135* gene was then inserted into the pGEX-6P-3 plasmid, as described previously (*7*). This manipulation generated the gene encoding the GST−Orf135 fusion protein. The nucleotide sequence of the gene was confirmed by sequencing, using a BigDye Terminator Cycle Sequencing Kit (Applera, Norwalk, CT) and an ABI model 377 DNA sequencer (Applera).

Purification of the GST−Orf135 Fusion Protein and Orf135. BL21(DE3) cells with the *GST-orf135* gene were cultured in 15 mL of LB medium containing amp at 37 °C until the turbidity at 610 nm reached 0.6. IPTG was added to a final concentration of 670 μM, and the *E. coli* culture was incubated at 37 °C for a further 2 h. The GST−Orf135 protein was purified as described previously (*15*). The purified proteins were analyzed by SDS−PAGE followed by Coomassie brilliant blue staining. They were visualized as single bands (data not shown).

The Orf135 protein without the GST tag was purified as described previously (*15*). The purified proteins were analyzed by SDS−PAGE, followed by Coomassie brilliant blue staining. Their purities and concentrations were determined by analysis of SDS−polyacrylamide gels using NIH Image, with bovine serum albumin as a protein for standard curves. Their purities were ≥94%.

Enzyme Assays. Enzymatic assays of the Orf135 protein was carried out as described previously (*7*, *16*). Detection was performed with UV absorbance at 272 nm (dCTP), 277 nm (5-Me-dCTP), or 292 nm (2-OH-dATP and 8-OH-dGTP). The Michaelis constant (K_m) and the catalytic constant (k_{cat}) were obtained from Lineweaver−Burk plots of the kinetic data (*17*). All reaction rates were linear during the course of the reaction.

Calculation of the Mutant Frequency. A single colony of JD22899, harboring the gene for either the GST or GST−Orf135 fusion protein, was taken from an LB agar plate with kanamycin (10 μg/mL), amp (50 μg/mL), and IPTG (2 μM), and was inoculated into 7 mL of LB medium containing kanamycin, amp, and IPTG. The *E. coli* culture was incubated at 37 °C until the turbidity at 570 nm reached 0.8, and then was diluted 10-fold with prewarmed LB medium containing amp and IPTG. When the turbidity at 570 nm reached 0.25, H_2O_2 was added to a final concentration of 2 mM, and the culture was incubated at 37 °C for 30 min. The culture was centrifuged at 2150*g* for 15 min at room temperature. The pellet thus obtained was resuspended in the same volume of prewarmed LB medium containing amp and IPTG, and then was diluted 2-fold with prewarmed LB medium containing amp and IPTG. The *E. coli* culture was incubated at 37 °C until the turbidity at 570 nm reached 0.85, and then was placed on ice for 10 min. A portion of the suspension was diluted with ice-cold LB medium, transferred onto an LB agar plate containing amp (a titer plate), and incubated at 37 °C for 12 h. Another portion of the suspension was transferred onto an LB agar plate containing rifampicin (100 μg/mL) and amp (a selection plate) and was incubated at 37 °C for 20 h. The mutant frequency was calculated according to the number of colonies on the titer and selection plates.

RESULTS

Amino Acid Residues of the Orf135 Protein Possibly Involved in Nucleotide Binding. A certain degree of sequence homology has been noted between the *E. coli* MutT and mammalian MTH1 proteins in a homologous region, the phosphohydrolase module or MutT signature (*18*, *19*). However, the level of sequence identity between the two proteins outside of this region is as low as 9.3%. Nevertheless, the overall folds of the MutT and MTH1 proteins resemble each other (*12*). The level of sequence identity between the MutT and Orf135 proteins is relatively high (31%), and their structures may be similar. A homology model of the Orf135 protein was built, based on the structure of the MutT protein as a template, using MODELLER (*20*). Distance restraints derived from the coordinates of MutT and energy minimization using a CHARMM force field were implemented for the modeling. Its nucleotide binding pocket was proposed by comparison with the structure of the human MTH1 protein (*12*) and by substrate titration experiments monitoring the HSQC spectrum using heteronuclear NMR (see the Supporting Information). The modeled structure was consistent with the preliminary NOE data obtained from NMR measurements. This model suggests that the Glu-33, Arg-72, Arg-77, and Asp-118 residues of Orf135 are exposed on the surface of the putative base-binding pocket, and are possible candidates for residues interacting with the base (Figure 1). We thus planned to substitute these amino acid residues.

These Glu-33, Arg-72, Arg-77, and Asp-118 residues of Orf135 were replaced with Ala, and some amino acids were substituted with their related ones. These mutant genes were

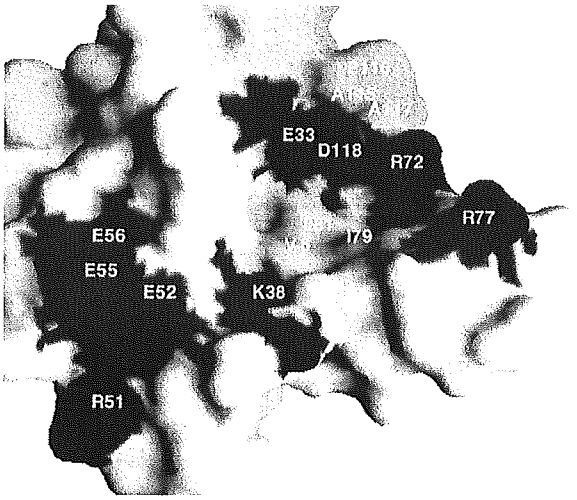

FIGURE 1: Model of the substrate-binding pocket of Orf135. This model was built based on the coordinates of the MutT protein, as described in the text. Acidic and basic residues are colored red and blue, respectively. Hydrophobic residues are colored yellow. The K38, R51, E52, E55, and E56 residues may be involved in phosphate binding, and thus were mutagenesis targets in the previous paper (*15*).

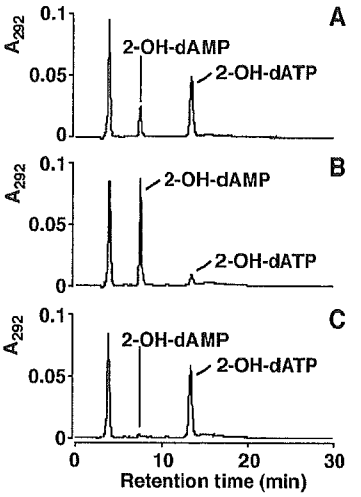

FIGURE 2: Hydrolysis of 2-OH-dATP by the GST−Orf135 protein, monitored by anion-exchange HPLC. 2-OH-dATP (20 μM) was incubated with 150 nM GST−Orf135 protein at 37 °C for 10 min, and analyzed as described in Experimental Procedures: (A) wt, (B) E33A, and (C) R72A. 2-OH-dAMP is 2-hydroxy-2′-deoxyadenosine 5′-monophosphate.

constructed by site-directed mutagenesis with mutagenic PCR primers (Table 1). The presence of the desired mutation was confirmed by sequencing.

Enzymatic Activities of the GST−Orf135 Protein Mutants. The *E. coli* Orf135 protein hydrolyzes 5-Me-dCTP and dCTP as well as 2-OH-dATP and 8-OH-dGTP (*7*, *8*), and the significance of the activities for the former two nucleotides is unknown. The 2-OH-dATPase activity of the Orf135 protein is particularly important, because a deficiency in the Orf135 protein affects the degree of mutation induction only in the case of 2-OH-dATP (*9*). First, various Orf135 mutants were tested for their abilities to hydrolyze these four deoxyribonucleotides. We used GST-fused Orf135 mutants purified by small-scale affinity chromatography in these screening experiments.

The 5-Me-dCTPase activities of these mutant proteins were examined with 50 μM 5-Me-dCTP and 50 nM proteins at 37 °C for 1 min. The other enzymatic activities were examined with a single deoxyribonucleotide (20 μM) and 150 nM proteins at 37 °C for 10 min. The product and the remaining substrate were quantitated by anion-exchange HPLC, as described previously (*7*, *16*). Interestingly, an increased rate of 2-OH-dATP hydrolysis was observed with the E33A, E33Q, and D118E mutant proteins (Figures 2 and 3). On the other hand, the R72A, D118A, and D118N mutants exhibited highly impaired 2-OH-dATPase activities. Likewise, the amino acid substitutions altered the hydrolyses of the other substrates to various degrees (Figure 3).

Interestingly, the replacement of Glu-33 with Ala enhanced the 2-OH-dATPase activity and suppressed the other three activities. The E33Q mutant displayed 2-OH-dATPase activity that was lower than that of E33A but higher than that of the wt protein. The 2-OH-dATPase activity of E33D was lower than that of the wt protein. The other three activities of these E33 mutant proteins were decreased, as compared to those of the wt protein. In particular, the dCTPase and 8-OH-dGTPase activities of these mutants were very low. The R72A protein exhibited suppressed 2-OH-dATPase and enhanced dCTPase activities, and the R72K protein had enzymatic activities similar to those of the wt protein. The substitution of Arg-77 with Ala only slightly affected the hydrolyzing activity of the Orf135 protein, thus excluding the possibility that the side chain of this Arg residue is important in base recognition. The D118A protein exhibited enhanced 8-OH-dGTPase activity, while the other activities were decreased. On the other hand, D118E lost the 8-OH-dGTPase activity, but its 2-OH-dATPase activity was higher than that of the wt protein. The D118N protein lost the 2-OH-dATPase activity but retained the other three activities. Interestingly, 8-OH-dGDP was produced by D118A and D118N. These results suggest that Glu-33, Arg-72, and Asp-118 are involved in base recognition, and the four substrates interacted with these residues in various ways.

The E33A, R72A, D118A, D118E, and D118N mutants were selected at this stage for further analyses of their activities in vitro.

Detailed Analyses of Mutant Orf135 Protein Activities toward Various Deoxyribonucleotides. The five Orf135 mutant proteins thus selected were purified after removal of the GST moiety. They were incubated with 2-OH-dATP and 8-OH-dGTP, as well as 5-Me-dCTP and dCTP (Figure 4). The 5-Me-dCTPase activity was measured with 100 μM 5-Me-dCTP and 15 nM protein, and the reaction mixtures were incubated at 37 °C for 2 min. The other enzymatic activities were examined with a single deoxyribonucleotide (20 μM) and 150 nM proteins at 37 °C for 10 min. Overall, as expected, the results obtained with the mutant proteins without the GST tag were similar to those obtained with the proteins containing the GST tag. The E33A mutant exhibited enhanced 2-OH-dATPase and drastically reduced 5-Me-dCTPase activities. Enhanced dCTPase and reduced 2-OH-dATPase activities were observed with the R72A protein. The D118A, D118E, and D118N mutant proteins displayed 2-OH-dATPase and 8-OH-dGTPase activities that were highly characteristic of the individual mutants. In the case

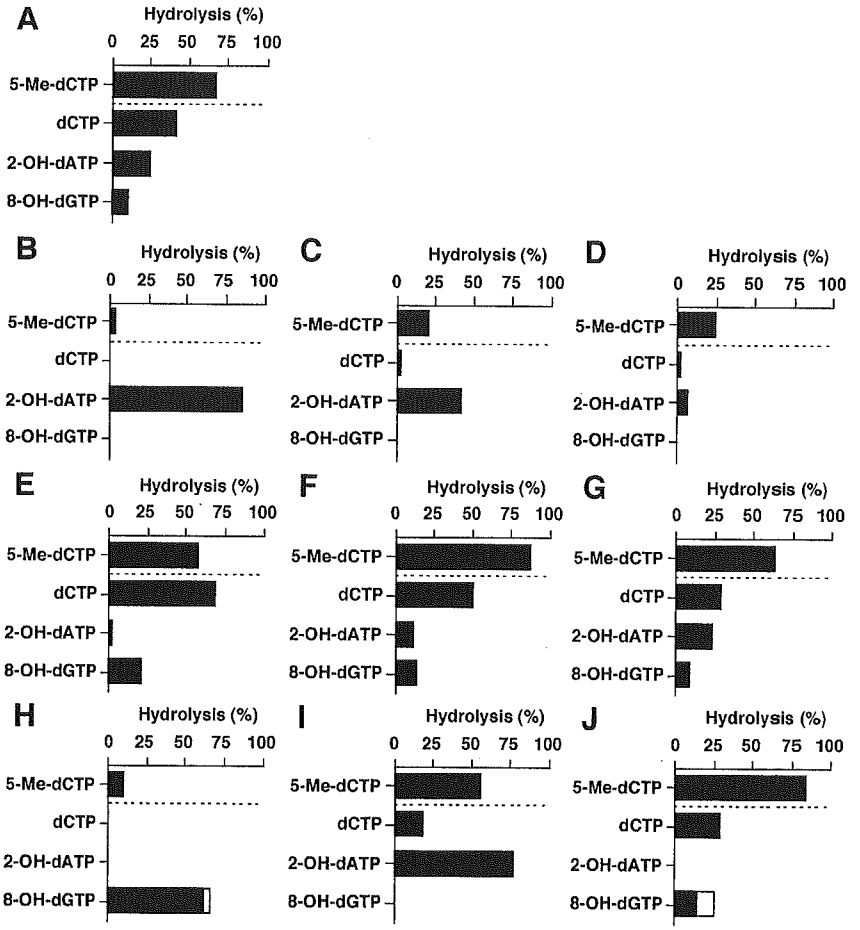

FIGURE 3: Hydrolysis of deoxyribonucleoside triphosphates by GST−Orf135 mutant proteins. 5-Me-dCTP (50 μM) was incubated with 50 nM GST−Orf135 protein at 37 °C for 1 min. dCTP, 2-OH-dATP, or 8-OH-dGTP (20 μM) was incubated with 150 nM GST−Orf135 protein at 37 °C for 10 min. The hydrolysis percentage was measured by HPLC, as described in Experimental Procedures: (A) wt, (B) E33A, (C) E33Q, (D) E33D, (E) R72A, (F) R72K, (G) R77A, (H) D118A, (I) D118E, and (J) D118N. The horizontal axis indicates the hydrolysis percentage for the total substrate added. Experiments were carried out at least in duplicate, and the mean values are represented. The empty boxes in panels H and J represent the percentage of 8-OH-dGDP.

of D118A, 8-OH-dGDP was not detected under the conditions described above (20 μM 8-OH-dGTP), in contrast to the case of D118A with the GST tag (Figures 3H and 4D). The production of 8-OH-dGDP was observed when a higher concentration of 8-OH-dGTP was used (data not shown).

The Michaelis constant (K_m) and the catalytic constant (k_{cat}) of the reactions catalyzed by the wt and mutant proteins were calculated (Table 2). Some kinetic parameters were not calculated, since the severely impaired activities made it difficult to determine the amount of product. In the case of the D118A mutant protein, 8-OH-dGDP was also produced, and the kinetic parameters were determined by considering both 8-OH-dGDP and 8-hydroxy-dGMP as the "product".

The K_m and k_{cat} values of E33A for 5-Me-dCTP were 8-fold larger and 13-fold smaller than those of the wt protein, respectively, resulting in a 100-fold reduced k_{cat}/K_m value. In contrast, the k_{cat} value of E33A for 2-OH-dATP was 8-fold larger than that of the wt protein. The K_m and k_{cat} values of D118A for 5-Me-dCTP were 9-fold larger and 4-fold smaller than those of the wt protein, respectively, resulting in a 34-fold reduced k_{cat}/K_m value. In contrast, the K_m and k_{cat} values of this mutant for 8-OH-dGTP were 2-fold smaller and 3-fold larger than those of the wt protein, respectively, resulting in the 6-fold increased k_{cat}/K_m value. The replacement of Asp-118 with Glu decreased the K_m value for 2-OH-dATP by 5-fold and increased the k_{cat} value by 3-fold. The k_{cat}/K_m value of the this mutant for 2-OH-dATP was thus 13-fold larger than that of the wt protein.

Mutation Suppression by Orf135 Mutant Proteins. A deficiency in the Orf135 protein causes an increase in the H_2O_2-induced mutation frequency (*9*). We then examined whether expression of the mutant proteins used in this study suppressed the H_2O_2-induced mutations. Plasmid DNAs containing the gene for either GST or the GST−Orf135 fusion protein were transfected into the *orf135*$^-$ strain. The expression of these genes was induced by IPTG treatment, and the protein production in the cells was confirmed by SDS−PAGE (data not shown). The amounts of GST or GST−Orf135 fusion proteins produced in cells were similar under the culture conditions that were used. These cells were treated with 2 mM H_2O_2, and their *rpoB* mutant frequencies were measured.

The expression of most of the tested mutant Orf135 proteins in the *orf135*$^-$ strain reduced the H_2O_2-induced mutant frequency, as compared with that of the GST protein (Figure 5). The expression of the E33A, E33Q, R72A, R72K,

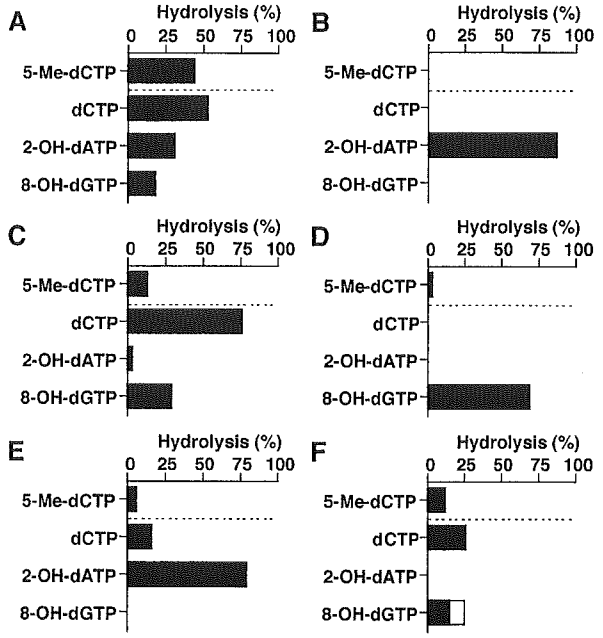

FIGURE 4: Hydrolysis of deoxyribonucleoside triphosphates by purified Orf135 mutant proteins without the GST tag. 5-Me-dCTP (100 μM) was incubated with 15 nM Orf135 at 37 °C for 2 min. dCTP, 2-OH-dATP, or 8-OH-dGTP (20 μM) was incubated with 150 nM GST−Orf135 protein at 37 °C for 10 min. The hydrolysis percentage was measured by HPLC, as described in Experimental Procedures: (A) wt, (B) E33A, (C) R72A, (D) D118A, (E) D118E, and (F) D118N. The horizontal axis indicates the hydrolysis percentage for the total substrate added. Experiments were carried out at least in duplicate, and the mean values are represented. The empty box in panel F represents the percentage of 8-OH-dGDP.

Table 2: Kinetic Parameters of Deoxyribonucleotides for the Orf135 Proteins[a]

Orf135	substrate	K_m (mM)	k_{cat} (s^{-1})	k_{cat}/K_m[b] (mM^{-1} s^{-1})
wt[c]	5-Me-dCTP	0.028	35	1300 (1.00)
	dCTP	0.99	6.3	6.4 (1.00)
	2-OH-dATP	0.027	0.17	6.4 (1.00)
	8-OH-dGTP	0.41	0.89	2.2 (1.00)
E33A	5-Me-dCTP	0.22	2.8	13 (0.01)
	2-OH-dATP	0.067	1.42	21 (3.28)
R72A	5-Me-dCTP	0.015	11	780 (0.60)
	dCTP	0.65	8.8	14 (2.19)
	8-OH-dGTP	0.31	1.4	4.6 (2.09)
D118A	5-Me-dCTP	0.24	9.1	38 (0.03)
	8-OH-dGTP	0.19	2.7	14 (6.36)
D118E	5-Me-dCTP	0.0069	6.5	944 (0.73)
	dCTP	0.93	2.1	2.3 (0.36)
	2-OH-dATP	0.0055	0.45	82 (12.81)
D118N	5-Me-dCTP	0.0057	7.7	1400 (1.08)
	dCTP	0.77	2.7	3.5 (0.55)

[a] Experiments were carried out at least in duplicate, and the mean values are represented. [b] Values relative to that of wt are shown in parentheses. [c] Data from ref *15*.

and D118A mutant proteins in the *orf135*$^-$ strain seemed to reduce the H_2O_2-induced mutation frequency.

DISCUSSION

Nakabeppu and his collaborators substituted the Trp-117 and Asp-119 residues of the MTH1 protein, and were able to "separate" its 8-OH-dGTPase and 2-OH-dATPase activities (*21*). In a subsequent study, they showed that both activities were important for the suppression of cell dysfunction and the delayed cell death of MTH1-null mouse embryo fibroblast cells, using these mutant MTH1 proteins (*11*). We carried out a mutagenesis study of the Orf135 protein, which has 2-OH-dATPase, 8-OH-dGTPase, dCTPase, and 5-Me-dCTPase activities, to identify the important amino acid residues for the recognition of each deoxyribonucleotide, and to examine which activities are important for the suppression of reactive oxygen species-induced mutations.

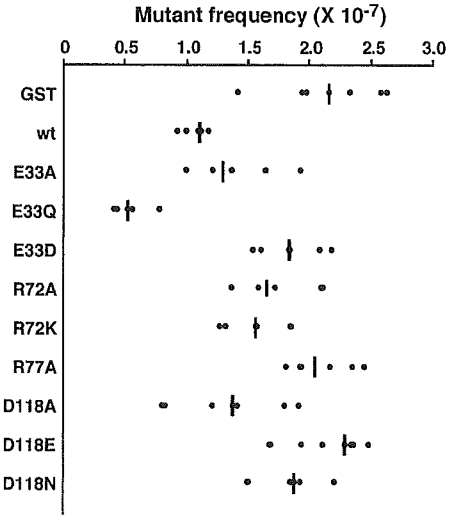

FIGURE 5: Suppression of H_2O_2-induced mutations by expression of the recombinant Orf135 protein. The *orf135*$^-$ *E. coli* strains, harboring a plasmid for GST or the GST−Orf135 protein, were treated with 2 mM H_2O_2, as described in Experimental Procedures. Experiments were carried out five to seven times. Filled circles represent each datum. Bars represent medians.

One of the objectives of this study was to examine the role of the amino acid residues in the putative nucleotide binding pocket of the Orf135 protein. This nucleotide binding pocket was proposed by a comparison of an Orf135 protein model with the human MTH1 protein structure (Figure 1) (*12*). We focused on the Glu-33, Arg-72, Arg-77, and Asp-118 residues, which were suggested to be exposed on the surface of the putative base-binding pocket.

The substitution of the Glu-33 residue of the Orf135 protein affected its activities to various degrees (Figure 3). The dCTPase and 8-OH-dGTPase activities were almost completely abolished, and the 5-Me-dCTPase activity was also reduced. Thus, this Glu residue may favorably interact with these three deoxyribonucleotides. The replacement of this residue with Ala and Gln increased the 2-OH-dATPase activity, and the E33D mutant exhibited reduced 2-OH-dATPase activity. These results suggest that the Glu-33 residue unfavorably interacts with 2-OH-dATP, because of the presence of a carboxyl (COO^-) group. The corresponding residue of the MTH1 protein is Asn-33. This residue was suggested to be important for nucleotide binding, because its side chain is exposed in the binding pocket (*12*). A site-directed mutagenesis study indicated that the presence of the side chain carbonyl (C=O) group at this position is important for recognizing 2-OH-dATP (*12*). The N33A MTH1 mutant exhibited 14% of the wt 8-OH-dGTP activity, whereas the N33E mutation totally abolished the 8-OH-dGTPase activity. In this case, the carboxyl group of this Glu may unfavorably interact with 8-OH-dGTP.

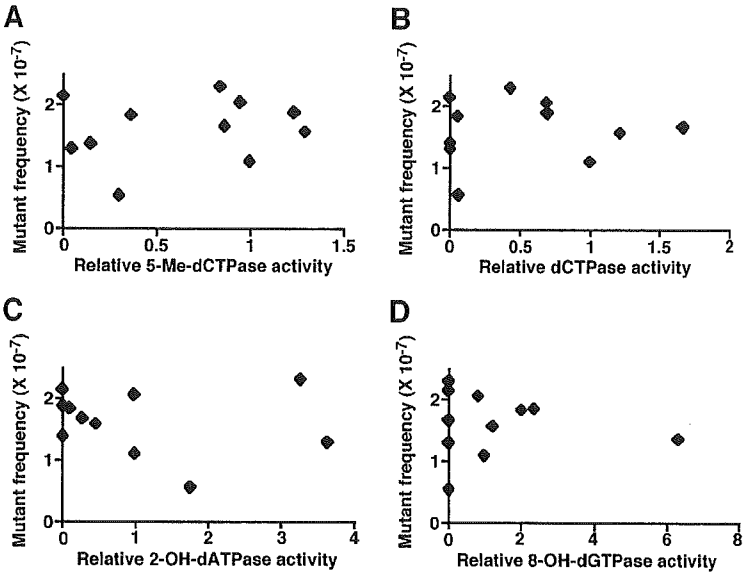

FIGURE 6: Correlation between the enzymatic activities of the GST−Orf135 and GST proteins and the *rpoB* mutant frequency. The relative activity was defined as described in the text: (A) 5-Me-dCTPase activity, (B) dCTPase activity, (C) 2-OH-dATPase activity, and (D) 8-OH-dGTPase activity.

The R72A mutant displayed increased dCTPase and reduced 2-OH-dATPase activities, suggesting favorable and unfavorable interactions, respectively, with 2-OH-dATP and dCTP. Since the R72K mutant had activities similar to those of the wt protein, these interactions may depend on the positive charge of the 72nd residue. The substitution of the Arg-77 residue affected the enzymatic activities only slightly, excluding the possibility that this Arg side chain is important in substrate binding. The Arg-78 residue of the MutT protein may interact with 8-OH-dGTP by hydrogen bonding (*22*). However, the substitution of the 72nd Arg residue of Orf135 with Ala or Lys did not affect the 8-OH-dGTPase activity drastically, indicating little, if any, interaction occurs between Arg-72 and 8-OH-dGTP.

The replacement of the Asp-118 residue generated quite interesting results (Figures 3 and 4). The D118A and D118N mutations almost completely abolished the 2-OH-dATPase activity. On the other hand, the D118E mutant displayed a 2-OH-dATPase activity higher than that of the wt protein (13-fold in the k_{cat}/K_m values, Table 2). In marked contrast, the 8-OH-dGTP hydrolyzing activity was diminished in the case of D118E, and the D118A and D118N proteins had increased 8-OH-dGTPase activity. Thus, the carboxyl (COO^-) group (negative charge) of this Asp residue appeared to contribute to 2-OH-dATP binding and to suppress 8-OH-dGTP binding. The 5-Me-dCTP and dCTPase activities were drastically impaired by the substitution of Asp-118 with Ala. The D119A mutant of MTH1 exhibited approximately half of the wt activity for 8-OH-dGTP, but had almost no activity for 2-OH-dATP, and the activities of the D119N mutant were similar to those of D119A (*21*). These results suggest that the charged carboxyl (COO^-) group of the side chain, but not the carbonyl (C=O) group, is crucial for discriminating 2-OH-dATP. Thus, Asp-118 of Orf135 and Asp-119 of MTH1 may interact with 2-OH-dATP in a very similar fashion. On the other hand, the charged carboxyl (COO^-) group of the Asp-118 residue in Orf135 unfavorably interacts with 8-OH-dGTP, although the Asp-119 residue in MTH1 does not seem to be very important for 8-OH-dGTP binding. In contrast, the Asn-119 residue of MutT seems to interact with 8-OH-dGTP by hydrogen bonding (*22*).

Intriguingly, the D118A and D118N mutants hydrolyzed 8-OH-dGTP to 8-OH-dGDP. Experiments using ^{18}O-enriched water revealed that the β-phosphorus atom of the substrate is attacked by water and the substrate Pα−Pβ bond is subsequently cleaved during the reactions by the MutT, Orf17, and MTH1 proteins (*12*, *23*, *24*). The Orf135 protein probably hydrolyzes the substrate nucleotides by the same mechanism. The emergence of 8-OH-dGDP as a product suggests the cleavage of the substrate Pβ−Pγ bond, followed by the attack of a water molecule on the β- and/or γ-phosphorus atom of the substrate during the reactions by these mutant proteins. The D118A and D118N mutants possessed 8-OH-dGDPase activities, and their total 8-OH-dGTPase activities were higher than their 8-OH-dGDPase activities (data not shown). Thus, more than half of the 8-hydroxy-dGMP produced by these mutant proteins was derived from the same mechanism as that of the wt enzyme, which possibly involves the nucleophilic attack of a water molecule on the β-phosphorus atom and the subsequent cleavage of the substrate Pα−Pβ bond. The substitution of Asp-118 with Ala or Asn might alter the local structure of the binding pocket, and the hydrolysis reaction may follow different pathways.

The other objective of this study was to examine the suppression of the mutagenesis induced by oxidatively damaged DNA precursors, by the mutant proteins with various substrate specificities. Previously, we reported that the Orf135 protein could hydrolyze deoxyribonucleotides, such as 2-OH-dATP, and that the expression of the recombinant Orf135 protein reduced the frequencies of both the H_2O_2-induced and spontaneous mutations (*7*, *9*).

The 5-Me-dCTPase, dCTPase, 2-OH-dATPase, and 8-OH-dGTPase activities of each mutant protein with the GST tag were normalized to those of the wt protein (wt = 1.0). We then examined the relationship between the H_2O_2-induced

mutant frequencies and the relative enzymatic activities of the mutant GST−Orf135 proteins in vitro (Figures 3 and 5). As shown in panels A, B, and D Figure 6, no correlation exists among the 5-Me-dCTPase, dCTPase, and 8-OH-dGTPase activities and the H_2O_2-induced mutant frequencies. Statistically significant correlation exists only between the H_2O_2-induced mutant frequencies and the 2-OH-dATPase activity (0−1.8 of relative activity, Figure 6C). The Pearson's correlation coefficient was calculated to be −0.71, which is statistically significant ($P < 0.05$). Thus, the results of these experiments may suggest that the 2-OH-dATPase activity of the Orf135 protein contributes to the suppression of the reactive oxygen species-elicited mutagenesis derived from oxidized deoxyribonucleotide(s) in *E. coli* cells. However, expression of the two mutants, E33A and D118E, did not suppress the H_2O_2-induced mutations. The actual reasons for these exceptions are unknown. These proteins may be unstable upon being treated with H_2O_2.

Tassotto and Mathews tried to measure the amount of 8-OH-dGTP in *E. coli*, and concluded that its intracellular concentration is below 0.34 μM (the limit of detection) (*25*). This failure to detect 8-OH-dGTP in extracts of *mutT* strains cast some doubt on the expected MutT function. However, the ratio of 0.34 μM 8-OH-dGTP to the estimated concentration of dGTP in the bacterium (100 μM) (*26*) is 3.4×10^{-3}, and this ratio appears to be too high when the in vivo situation is considered. Thus, their result did not deny roles of the nucleotide pool sanitization. In contrast, deficiencies in the *E. coli* MutT and Orf135 and mammalian MTH1 proteins result in increased mutation frequency and enhanced tumor formation, indicating the importance of the nucleotide pool sanitization (*5*, *6*, *9*). Thus, oxidatively damaged DNA precursors appear to be formed in cells and be involved in mutagenesis by ROS.

ACKNOWLEDGMENT

We thank Drs. Yoshihiro Yamamoto and Takeyoshi Miki for *E. coli* strain JD22899.

SUPPORTING INFORMATION AVAILABLE

Structures of MutT, MTH1, and Orf135. This material is available free of charge via the Internet at http://pubs.acs.org.

REFERENCES

1. Sekiguchi, M., and Tsuzuki, T. (2002) Oxidative nucleotide damage: Consequences and prevention, *Oncogene 21*, 8895−8904.
2. Kamiya, H. (2003) Mutagenic potentials of damaged nucleic acids produced by reactive oxygen/nitrogen species: Approaches using synthetic oligonucleotides and nucleotides, *Nucleic Acids Res. 31*, 517−531.
3. Maki, H., and Sekiguchi, M. (1992) MutT protein specifically hydrolyses a potent mutagenic substrate for DNA synthesis, *Nature 355*, 273−275.
4. Mo, J.-Y., Maki, H., and Sekiguchi, M. (1992) Hydrolytic elimination of a mutagenic nucleotide, 8-oxodGTP, by human 18-kilodalton protein: Sanitization of nucleotide pool, *Proc. Natl. Acad. Sci. U.S.A. 89*, 11021−11025.
5. Yanofsky, C., Cox, E. C., and Horn, V. (1966) The unusual mutagenic specificity of an *E. coli* mutator gene, *Proc. Natl. Acad. Sci. U.S.A. 55*, 274−281.
6. Tsuzuki, T., Egashira, A., Igarashi, H., Iwakuma, T., Nakatsuru, Y., Tominaga, Y., Kawate, H., Nakao, K., Nakamura, K., Ide, F., Kura, S., Nakabeppu, Y., Katsuki, M., Ishikawa, T., and Sekiguchi, M. (2001) Spontaneous tumorigenesis in mice defective in the MTH1 gene encoding 8-oxo-dGTPase, *Proc. Natl. Acad. Sci. U.S.A. 98*, 11456−11461.
7. Kamiya, H., Murata-Kamiya, N., Iida, E., and Harashima, H. (2001) Hydrolysis of oxidized nucleotides by the *Escherichia coli* Orf135 protein, *Biochem. Biophys. Res. Commun. 288*, 499−502.
8. O'Handley, S. F., Dunn, C. A., and Bessman, M. J. (2001) Orf135 from *Escherichia coli* is a Nudix hydrolase specific for CTP, dCTP, and 5-methyl-dCTP, *J. Biol. Chem. 276*, 5421−5426.
9. Kamiya, H., Iida, E., Murata-Kamiya, N., Yamamoto, Y., Miki, T., and Harashima, H. (2003) Suppression of spontaneous and hydrogen peroxide-induced mutations by a MutT-type nucleotide pool sanitization enzyme, the *Escherichia coli* Orf135 protein, *Genes Cells 8*, 941−950.
10. Inoue, M., Kamiya, H., Fujikawa, K., Ootsuyama, Y., Murata-Kamiya, N., Osaki, T., and Kasai, H. (1998) Induction of chromosomal gene mutations in *Escherichia coli* by direct incorporation of oxidatively damaged nucleotides, *J. Biol. Chem. 273*, 11069−11074.
11. Yoshimura, D., Sakumi, K., Ohno, M., Sakai, Y., Furuichi, M., Iwai, S., and Nakabeppu, Y. (2003) An oxidized purine nucleoside triphosphatase, MTH1, suppresses cell death caused by oxidative stress, *J. Biol. Chem. 278*, 37965−37973.
12. Mishima, M., Sakai, Y., Itoh, N., Kamiya, H., Furuichi, M., Takahashi, M., Yamagata, Y., Iwai, S., Nakabeppu, Y., and Shirakawa, M. (2004) Structure of human MTH1: A NUDIX family hydrolase that selectively degrades oxidized purine nucleoside triphosphates, *J. Biol. Chem. 279*, 33806−33815.
13. Cheng, K. C., Cahill, D. S., Kasai, H., Nishimura, S., and Loeb, L. A. (1992) 8-Hydroxyguanine, an abundant form of oxidative DNA damage, causes G→T and A→C substitutions, *J. Biol. Chem. 267*, 166−172.
14. Kamiya, H., and Kasai, H. (1995) Formation of 2-hydroxydeoxyadenosine triphosphate, an oxidatively damaged nucleotide, and its incorporation by DNA polymerases, *J. Biol. Chem. 270*, 19446−19450.
15. Kamiya, H., Iida, E., and Harashima, H. (2004) Important amino acids in the phosphohydrolase module of *Escherichia coli* Orf135, *Biochem. Biophys. Res. Commun. 323*, 1063−1068.
16. Fujikawa, K., Kamiya, H., Yakushiji, H., Fujii, Y., Nakabeppu, Y., and Kasai, H. (1999) The oxidized forms of dATP are substrates for the human MutT homologue, the hMTH1 protein, *J. Biol. Chem. 274*, 18201−18205.
17. Fersht, A. (1977) in *Enzyme Structure and Mechanism*, pp 91−92, Freeman, San Francisco.
18. Nakabeppu, Y. (2001) Molecular genetics and structural biology of human MutT homolog, MTH1, *Mutat. Res. 477*, 59−70.
19. Bessman, M. J., Frick, D. N., and O'Handley, S. F. (1996) The MutT proteins or "Nudix" hydrolases, a family of versatile, widely distributed, "housecleaning" enzymes, *J. Biol. Chem. 271*, 25059−25062.
20. Sali, A., and Blundell, T. L. (1993) Comparative protein modelling by satisfaction of spatial restraints, *J. Mol. Biol. 234*, 779−815.
21. Sakai, Y., Furuichi, M., Takahashi, M., Mishima, M., Iwai, S., Shirakawa, M., and Nakabeppu, Y. (2002) A molecular basis for the selective recognition of 2-hydroxy-dATP and 8-oxo-dGTP by human MTH1, *J. Biol. Chem. 277*, 8579−8587.
22. Massiah, M. A., Saraswat, V., Azurmendi, H. F., and Mildvan, A. S. (2003) Solution structure and NH exchange studies of the MutT pyrophosphohydrolase complexed with Mg^{2+} and 8-oxo-dGMP, a tightly bound product, *Biochemistry 42*, 10140−10154.
23. O'Handley, S. F., Frick, D. N., Bullions, L. C., Mildvan, A. S., and Bessman, M. J. (1996) *Escherichia coli orf17* codes for a nucleoside triphosphate pyrophosphohydrolase member of the MutT family of proteins, *J. Biol. Chem. 271*, 24649−24654.
24. Weber, D. J., Bhatnagar, S. K., Bullions, L. C., Bessman, M. J., and Mildvan, A. S. (1992) NMR and isotopic exchange studies of the site of bond cleavage in the MutT reaction, *J. Biol. Chem. 267*, 16939−16942.
25. Tassotto, M. L., and Mathews, C. K. (2002) Assessing the metabolic function of the MutT 8-oxodeoxyguanosine triphosphatase in *Escherichia coli* by nucleotide pool analysis, *J. Biol. Chem. 277*, 15807−15812.
26. Mathews, C. K. (1972) Biochemistry of deoxyribonucleic acid-defective amber mutants of bacteriophage T4. 3. Nucleotide pools, *J. Biol. Chem. 247*, 7430−7438.

BI048071O

Disassembling and Bleaching of Chloride-Free *pharaonis* Halorhodopsin by Octyl-β-glucoside

Megumi Kubo,[‡] Maki Sato,[‡] Tomoyasu Aizawa,[‡] Chojiro Kojima,[§] Naoki Kamo,[∥] Mineyuki Mizuguchi,[⊥] Keiichi Kawano,[‡] and Makoto Demura*[,‡]

Division of Biological Sciences, Graduate School of Science, Hokkaido University, 060-0810, Japan, Laboratory of Biophysics, Graduate School of Biological Sciences, Nara Institute of Science and Technology, 8916-5 Takayama, Ikoma, Nara 630-0192, Japan, Graduate School of Pharmaceutical Sciences, Hokkaido University, Sapporo 060-0812, Japan, and Faculty of Pharmaceutical Sciences, Toyama Medical and Pharmaceutical University, Toyama 930-0194, Japan

Received June 13, 2005; Revised Manuscript Received July 29, 2005

ABSTRACT: *Natronomonas* (*Natronobacterium*) *pharaonis* halorhodopsin (NpHR) is a transmembrane, seven-helix retinal protein of the archaeal bacterium and acts as an inward light-driven chloride ion pump in the membrane. The denaturation process of NpHR solubilized with *n*-octyl-β-D-glucopyranoside (OG) was investigated to clarify the effects of the chloride ion and pH on the stability and bleaching of the NpHR chromophore. Initially, active NpHR solubilized with *n*-dodecyl-β-D-maltopyranoside (DM) was obtained from the recombinant halo-opsin (NpHO), which was expressed in *Escherichia coli* cells, by adding all-*trans* retinal to the medium. Apparent molecular weight of the active NpHR solubilized with DM, which was determined by gel-filtration chromatography and dynamic light scattering, indicated the oligomeric state. The bleaching of NpHR in the dark by the addition of 50 mM OG in the presence and absence of chloride was investigated. In the presence of 256 mM NaCl, the bleaching of NpHR was strongly inhibited. On the other hand, in the absence of NaCl, an immediate decrease of absorbance at 600 nm was observed. Stopped-flow rapid-mixing analysis clarified the bleaching process in the absence of chloride as DM−NpHR (oligomeric) ↔ OG−NpHR (disassembled) ↔ intermediate → NpHO and free retinal, and each rate constant were determined. The formation of an intermediate (450 nm) in the dark was found to be strongly dependent on pH, as well as anion and detergent concentrations. The disassembling and protonation of a Schiff base corresponding to the bleaching intermediate is also discussed.

Halorhodopsin (HR),[1] bacteriorhodopsin (bR), sensory rhodopsin I, and phoborhodopsin (sensory rhodopsin II) are transmembrane, seven-helix retinal proteins in the membrane of the archaeal bacterium (*1*). These four proteins have the same global fold, and an all-*trans* retinal chromophore binds to a conserved lysine residue on the seventh helix via a protonated Schiff base. bR (an outward-directed, light-driven proton pump) has become one of the most typical model systems for studying the membrane protein structure, folding, bioenergetics, photochemistry, and mechanism of proton transport (*2*, *3*).

On the other hand, HRs (an inward-directed, light-driven chloride ion pump) from *Halobacterium salinarum* (*4*, *5*) and *Natronomonas* (*Natronobacterium*) *pharaonis* (*6*, *7*) alone have been extensively studied; however, several HRs have been identified and reported (*8*−*10*). In 2000, the crystalline structure of the *H. salinarum* HR (HsHR) determined at 1.8 Å resolution had been reported (*11*). Because the primary structures of HsHR and *N. pharaonis* HR (NpHR) are very highly homologous (66%) (*12*), their tertiary structures would be expected to be conserved. One of the greatest advantages of using NpHR is its stability, which is higher than that of HsHR in a chloride-free system. In addition, an *Escherichia coli* expression system for the archaeal retinal proteins including NpHR was recently reported (*13*, *14*). In this expression system, the use of a histidine-tagged protein rendered it possible to purify the retinal proteins in only one step, thereby allowing simple and large-scale preparation (*15*−*17*). In the case of recombinant NpHR purified from *E. coli* membrane, the visible circular dichroism (CD) exciton coupling corresponding to the self-assembling structure having a two-dimensional crystalline is observed to be the same as that purified from the *N. pharaonis* membrane.

The HsHR during the dark and light adaptations in NaCl contains about 45 and 75% all-*trans* configuration (*18*). In Na_2SO_4, there is no adaptation, and the all-*trans* content of the sample was shown to be approximately 67% (*19*). In contrast, in NpHR, the all-*trans* content of the preparation is known to remain constant at 85% under all conditions tested (different salts and light illumination) (*7*, *19*). The photocycle of NpHR has intermediates analogous to those of bR (*20*). However, in the photocycle of NpHR, no intermediate corresponding to the M (deprotonated Schiff

* To whom correspondence should be addressed. Telephone/fax: +81-11-706-2771. E-mail: demura@sci.hokudai.ac.jp.
‡ Graduate School of Science, Hokkaido University.
§ Nara Institute of Science and Technology.
∥ Graduate School of Pharmaceutical Sciences, Hokkaido University.
⊥ Toyama Medical and Pharmaceutical University.

[1] Abbreviations: DM, *n*-dodecyl-β-D-maltopyranoside; OG, *n*-octyl-β-D-glucopyranoside; NpHR, halorhodopsin from *Natrononomas pharaonis*; HsHR, halorhodopsin from *Halobacterium salinarum*.

10.1021/bi0511235 CCC: $30.25
Published on Web 09/03/2005

base) is thought to exist (*6*). More recently, the roles played by putative anion-binding sites in the cytoplasmic and extracellular channels of NpHR have been investigated using the wild-type protein and various mutant proteins, all of which were functionally expressed in *E. coli* cells (*21*).

The thermal and photobleaching of bR and/or retinal-binding process from the apoprotein without a retinal (opsin) have been previously investigated in terms of the effects of light, ion species, temperature, pH, and detergents (*2*, *22*−*25*). In these experiments, the self-assembling states of bR have typically been monitored using visible CD spectroscopy. It is thought that, in the solubilized state and under light illumination, the purple membrane is disassembled into a monomeric state by *n*-octyl-*β*-D-glucopyranoside (OG); moreover, the stability of the membrane is considered to be much lower than that of the native structure (*24*). On the other hand, the process of retinal binding from bacterio-opsin to the intermediates in the detergent micelles has been reported from the visible absorption shift (*2*). However, to date, there has been no comparative study of the stability and refolding of the HR in detergent micelles.

In this paper, the denaturation process of *N. pharaonis* HR (NpHR) solubilized with OG was investigated to clarify the effects of the presence of chloride ion and pH on the stability and bleaching of the NpHR chromophore. We expressed histidine-tagged wild-type NpHR in *E. coli* cells and elucidated the reversible intermediate between the native and denaturized (bleached) structures in a nonionic detergent, OG, using stopped-flow rapid mixing. As mentioned above, NpHR and HsHR exhibit slight differences in stability in a chloride-free system, as well as in terms of light−dark adaptation and anion selectivity for pumping. Thus, it remains important to clarify the stability and assembly of NpHR under solubilized conditions. Gel-filtration chromatography and dynamic light-scattering (DLS) methods were also applied to measure the apparent molecular weight (*26*, *27*). On the basis of these experiments, the transient intermediate and changes in the number of associated NpHR molecules during the bleaching process are discussed below.

MATERIALS AND METHODS

Protein Expression and Purification of NpHR. The expression of the recombinant NpHR in *E. coli* [strain BL21 (DE3)] and purification procedures have been described previously (*15*). Fractions of the proteins separated with Ni-NTA-agarose (Qiagen, Hilden, Germany) were collected by elution (flow rate, 56 mL/h) with buffer A [50 mM Tris-HCl (pH 7.0), 300 mM NaCl, 150 mM imidazole, and 0.1% *n*-dodecyl-*β*-D-maltopyranoside (dodecyl maltoside, DM) (Dojindo Lab, Kumamoto, Japan)]. The samples were stored at 4 °C for 1 month, and then the supernatant (DM−NpHR complex) was collected by centrifugation (18000*g*, 20 min).

Preparation of the Anion-Deleted DM−NpHR Complex. The anion-deleted blue species of NpHR ($NpHR^{blue}$) were prepared by replacing buffer A with buffer B [10 mM 2-morpholinopropanesulfonic acid, MOPS (pH 7.0), and 0.1% DM] by passage over Sephadex-G 25 in a PD-10 column (8.3 mL; Amersham Pharmacia Biotech, Uppsala, Sweden) at a flow rate of 2 mL/min. After buffer exchange, the protein concentration was estimated using an excitation coefficient ϵ_{600} of 50 000 M^{-1} cm^{-1} (*28*).

Gel-Filtration Chromatography of the DM−NpHR Complex. Superdex 200 pg resin (Amersham Biosciences, Hilden, Germany) was applied to a chromatography column (inner diameter, 1.5 cm; height, 75 cm). The DM−NpHR complex was eluted (flow rate, 1 mL/3 min) with buffer [10 mM NaP_i (pH 8.0), 150 mM NaCl, and 0.1% DM]. The fractions were collected in a volume of 0.5−1.0 mL for each tube. The reference materials for the calibration curves were Blue Dextran 2000 (Amersham Biosciences, Hilden, Germany), which was used to determine the void volume and check the column packing, as well as several known standard substances, i.e., those in the Pharmacia Gel Filtration Kit [Thyroglobulin (MW 669 000), Ferritin (MW 440 000), and Catalase (MW 232 000), Amersham Biosciences, Hilden, Germany] and Albumin (MW 66 000), Ovalbumin (MW 44 000), and Chymotrypsinogen A (MW 13 700) (Sigma, St. Louis, MO). Fresh Blue Dextran 2000 solution (1.0 mg/mL) was prepared in the eluent buffer. The proper combination of standard substances was dissolved in the eluent buffer. The concentration of each protein ranged between 5 and 20 mg/mL (except for Ferritin, 1 mg/mL). The volume of these calibration solutions was 1−2% of the total gel bed volume (V_t). A calibration curve of K_{av} values versus log molecular weight was prepared according to the instruction manual. The K_{av} of each protein was calculated according to the following equation, $K_{av} = (V_e - V_o)/(V_t - V_o)$, where V_e is the elution volume for the protein and V_o is the column void volume, which is equal to the elution volume for Blue Dextran 2000. The absorbance of each fraction was measured using a Nanodrop ND-1000 spectrophotometer (NanoDrop Technologies, Inc., Rockland, DE) (path length, 1 mm).

DLS Measurements. The molecular mass of the DM micelle and the solubilized NpHR in DM was examined by DLS using DynaPro (Protein Solutions, Charlottesville, VA) at 20 °C. The buffer containing 0.1% DM, 10 mM MOPS (pH 7), NaCl (~100 mM−1 M) with and without 45 μM NpHR was centrifuged at 10 000 rpm for 10 min. The intensity of light (780 nm) scattered at an angle of 90° was measured. The measurement of the intensity of the light was repeated at least 10 times. The data were analyzed on the basis of the hydrodynamic radius, assuming that the particles were spherical and of standard density, using Dynamics 4.0 and DynaLS software, as described by Osawa et al. (*27*).

Time-Resolved Absorption Measurements. Time-resolved absorption changes caused by the manual mixing of chloride-free $NpHR^{blue}$ with OG were measured with a HITACHI U-2000 spectrophotometer (Hitachi, Tokyo, Japan) after the samples were mixed for 20 s in the 300−700 nm region at 25 °C using a single accumulation and a scanning speed of 800 nm/min. The measuring medium was buffer B, which contained various concentrations of NaCl. The path length of the optical cuvette was 10 mm. In the pH titration experiment, 10 mL of 6-Mix buffer [citric acid, MES, MOPS, Tricine, CHES, and CAPS] containing 0.1% DM was used.

Time-resolved absorption changes caused by the rapid mixing of chloride-free $NpHR^{blue}$ with OG were measured using an RA-2000 stopped-flow spectrophotometer (Otsuka Electronics, Osaka, Japan) with a dead time of 1.3 ms. The path length of the optical cell was 10 mm. The ratio of the mixing volumes of the protein and the 100 mM OG solutions was 1:1. The final concentrations of protein and OG were 4

μM and 50 mM, respectively. Rapid scan absorption changes in the 340−660 nm range were measured using a photodiode array at 1-s intervals after mixing, which gave the difference spectra caused by the addition of OG until 256 s after mixing. Singular value decomposition (SVD) treatment (*29*) was performed to determine the number of spectral components, as well as to remove the noise. Kinetic analysis and a global fitting were performed using the Igor Pro 3.14 software package (Wave Metrics, Lake Oswego, OR) (*17*).

Extraction of Retinal from NpHR and High-Performance Liquid Chromatography (HPLC) Analysis. After the addition of 50 mM OG to the NpHR samples for 0 s, 50 s, 30 min, and 3 h, the extraction of the retinal from the NpHR samples was carried out as described by Shimono and co-workers (*30*). A total of 100 μL of the samples was mixed with 300 μL of 90% methanol and 50 μL of 1 M hydroxylamine. After denaturation, retinal oxime was extracted by adding 800 μL of hexane under conditions of vigorous mixing. The emulsion was centrifuged with a hand-rotating centrifuge, and 50−200 μL of the upper phase was immediately separated by HPLC. A silica column (6 × 150 mm, YMC-0123, Yamamura, Japan) was used for HPLC with 12% (v/v) ethyl acetate and 0.12% (v/v) ethanol in hexane as a solvent at a flow rate of 1.0 mL/min, and the oximes were detected at 360 nm. All reagents were HPLC-grade reagents. The molar compositions of the retinal isomers were calculated from the areas of the peaks in the HPLC patterns. The extinction coefficients of all-*trans* and 13-*cis* retinaloximes (*31*) and that of the free retinal obtained in this study were used to estimate retinal composition. Assignment of the peaks was performed by comparing the peaks with those in the HPLC pattern from retinal oximes extracted by the same method from bR kept in the dark.

RESULTS

Estimation of the Apparent Molecular Weight of the DM−NpHR Complex. The purified NpHR on the Ni-NTA affinity column and the reference proteins for the calibration of molecular weight were fractionated by gel-filtration chromatography in the presence of 150 mM NaCl. The absorbance of these fractionations was observed at 280 and 578 nm (Figure 1). The absorbance at 578 nm could be attributed to the functional NpHR. On the other hand, the absorbance at 280 nm signified the total protein. The linear calibration was obtained as shown in the inset in Figure 1. The NpHR sample was separated into two peaks in elution volumes of 52 (void volume) and 63 mL when the absorbance was observed at 280 nm. In regard to the main peak (elution volume, 63 mL), absorbance at 578 nm was observed. This leads to a highly pure NpHR preparation with a ratio of 1.28 between an OD at 280 and 578 nm; these results agreed well with the reported value (1.25) for the purified NpHR obtained from the *N. pharaonis* membrane (*28*). Sodium dodecyl sulfate−polyacrylamide gel electrophoresis (SDS−PAGE) of these fractionations by this chromatographic approach was performed to confirm the molecular weight of the denatured proteins. A major band on SDS−PAGE with a mass of approximately 32 kDa was detected for both of the two peaks obtained with elution volumes of 52 and 63 mL (data not shown). These results suggest that the fractions eluted earlier were *pharaonis* halo-opsin (*p*HO), which does not retain a retinal inside the protein and is inactive. Nonreduced SDS−PAGE was also performed, because the NpHR has three cysteine residues. The results were identical to those obtained by SDS−PAGE under reduced conditions. Thus, it was concluded that the aggregation of the DM−NpHO complex was not ascribable to an intermolecular disulfide bond.

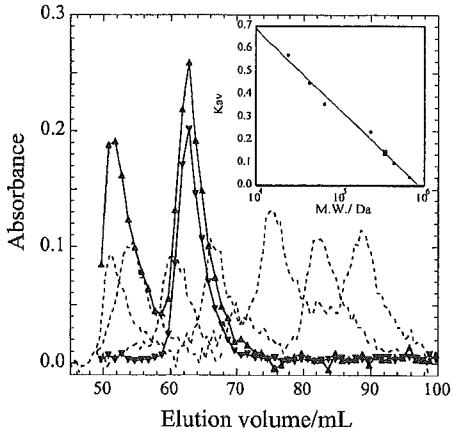

FIGURE 1: Absorbance at 280 nm (▲) and 578 nm (▼) of fractions collected by gel-filtration chromatography. The dotted lines show the absorbance at 280 nm of Blue Dextran 2000 and protein standards. (Inset) The calibration curve using the globular protein standards (●) on Superdex 200 pg. The apparent molecular weight of the DM−NpHR complex (■) was estimated by substituting K_{av}, which was calculated from the elution volume (V_e) for the calibration curve.

On the basis of the calibration of the apparent molecular weight of the eluted protein and the elution volume of each protein applied to this column (inset of Figure 1), the K_{av} of each protein was calculated (see the Materials and Methods). The K_{av} value of the main peak indicated that the apparent molecular weight of the DM−NpHR complex was approximately 340 kDa, which is larger than the molecular weight of the NpHR monomer (32 kDa). Moreover, the apparent molecular weight of the DM−NpHR complex and the DM micelles according to the DLS method was 400−430 and 66−100 kDa, under the assumption that the monomodal particles were spherical. Therefore, these results suggested the oligomeric state of the NpHR in the DM micelle system. This result was supported from previous reports of the visible CD exciton coupling, corresponding to the self-assembling structure having a two-dimensional crystalline (*15*, *21*).

Bleaching of DM−NpHR by OG in the Presence and Absence of the Chloride Ion. Figure 2 shows the change in the relative absorbance of chloride-free DM−NpHR^{blue} at λ_{max} (600 nm) after the addition of 0−50 mM OG at 25 °C in the dark. In the absence of OG, chloride-free DM−NpHR^{blue} did not exhibit a rapid decrease in absorbance. When DM−NpHR^{blue} was resolubilized to a 10 mM OG solution, the absorbance of NpHR^{blue} decreased; moreover, when DM−NpHR^{blue} was resolubilized to a concentration of more than 25 mM OG, it exhibited almost total bleaching within 1 h. These results were in agreement with the critical micelle concentration (cmc; 22 mM) of OG (*32*). Thus, we adopted a concentration of 50 mM OG in the following experiments. Interestingly, as shown in Figure 2, a biphasic denaturation curve in the absorbance at the initial resolubilizing step of NpHR from DM to OG micelle system was observed within 20 s when concentrations of OG exceeding

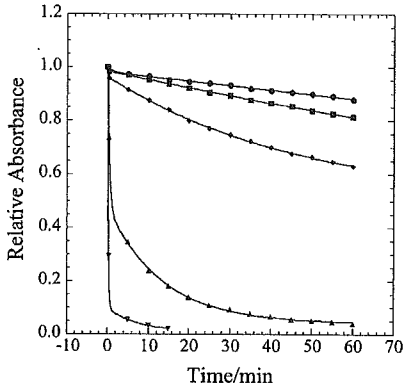

FIGURE 2: Changes in the relative absorbance at the maximum difference in the absorbance of chloride-free NpHR with the addition of 0 (●), 5 (■), 10 (◆), 25 (▲), and 50 (▼) mM OG. The wavelengths measured were 635, 620, 620, 600, and 600 nm, respectively. The concentration of NpHR was 4 μM. The final solution in the sample contained 0−50 mM OG, 2 mM DM, and 10 mM MOPS (pH 7.0).

10 mM were used. Decreasing the light scattering of the oligomeric DM−NpHR might have led to this result.

The bleaching of DM−NpHR by the addition of 50 mM OG in the presence and absence of chloride was also investigated as time-resolved absorption changes in the 300−700 nm region (Figure 3). These spectra were measured before the addition of OG and from 30 s to 1 h after the addition of OG. In the presence of 256 mM NaCl (Figure 3C), a small discrete change at the initial step and a subsequent slight decrease were observed. A similar degree of stability of NpHR in the presence of more than 64 mM NaCl was observed and is shown in Figure 4. These findings indicate that the bleaching of NpHR induced by the addition of OG was strongly inhibited by the local structure of the chromophore, which has a chloride-binding site. In the presence of 32 mM NaCl (Figure 3B), a gradual decrease in absorption at 580 nm and a concomitant increase in absorption at 380 nm were observed within this period of measurement. These two peaks did not indicate an unequivocal isosbestic point. However, in the absence of NaCl (Figure 3A), an immediate decrease initiated at 600 nm and an increase at 380 nm were observed. In addition, two isosbestic points were observed at 420 and 505 nm, as well as a broad peak between these isosbestic points, thereby suggesting the presence of a structural intermediate.

Structural Intermediate Obtained by the Bleaching of Chloride-Free NpHR^{blue}. To measure the spectral changes of chloride-free DM−NpHR^{blue} in the early stages after the addition of OG, a stopped-flow rapid-mixing technique was applied. Figure 5A shows a two-dimensional contour map of the spectral changes between 350 and 650 nm as a function of time after the addition of 50 mM OG. The interval used for measurement was 1 s. As shown in this figure, when chloride-free DM−NpHR^{blue} with a visible absorption at 600 nm was resolubilized with OG, the absorption peak at 380 nm was generated with a maximum peak at 450 nm. This result agrees with the detection of two isosbestic points (Figure 3A). Thus, it was concluded that, by the addition of OG, the chloride-free DM−NpHR^{blue} decreases as follows:

$$\text{DM−NpHR}^{blue} \rightarrow I_{450} \rightarrow I_{380} \quad (1)$$

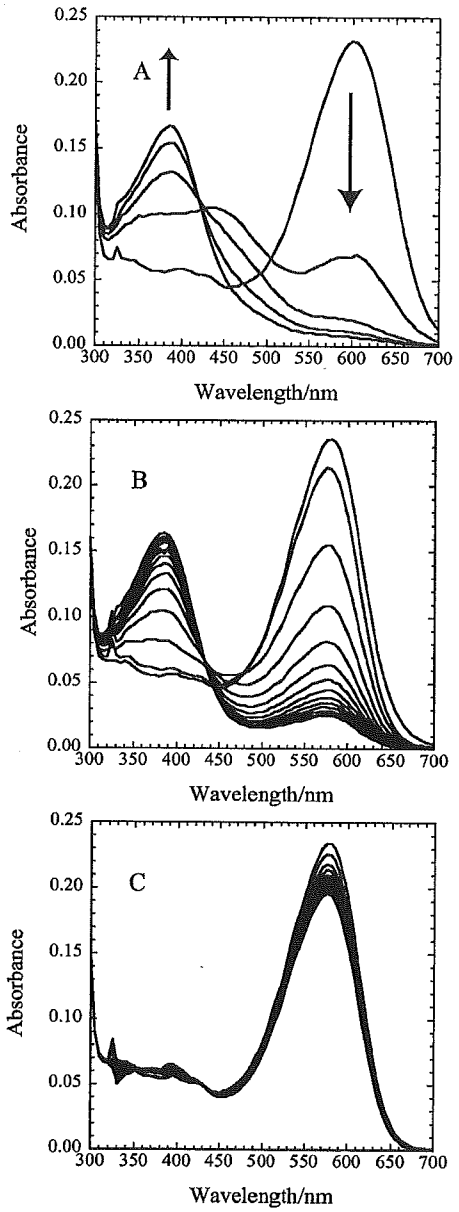

FIGURE 3: Changes in the absorption spectra of NpHR during the bleaching reaction by the addition of 50 mM OG at pH 7. The concentrations of NaCl were 0 mM (A), 32 mM (B), and 256 mM (C). The first spectrum obtained before the addition of OG, the second spectrum obtained after the addition of OG at 30 s, and the following spectra obtained in 5-min intervals until 1 h are shown. Noise was obtained in the region near 325 nm because of a change in the stray light-cutting filter used in the spectrometer. The final solution in the sample contained 50 mM OG, 2 mM DM, and 10 mM MOPS.

As mentioned above, it was found that the DM−NpHR is in the oligomeric state, and the addition of excess OG led to a discrete decrease in absorption as a result of a decrease in light scattering because of disassembling of the oligomeric state. In addition, we could observe a small decrease of the negative exciton band (600 nm) of visible CD spectrum at the beginning of exchange of DM and excess OG micelles, which corresponds to the intermolecular exciton coupling of NpHR chromophores (data not shown), suggesting disruption of the NpHR oligomer. Therefore, the reaction in

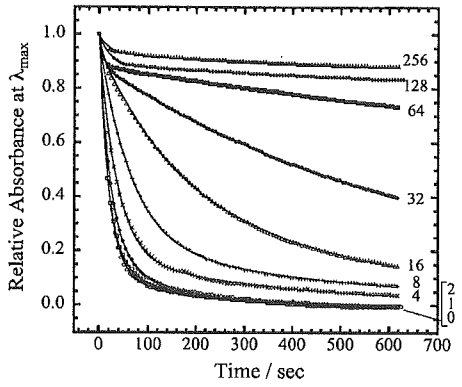

FIGURE 4: Decay curves of relative absorbance during the bleaching of NpHR at the λ_{max}. The numbers signify the concentration of chloride contained in each sample. NaCl concentrations, λ_{max}, and the identifiers are 0 mM (600 nm), ○; 1 mM (600 nm), □; 2 mM (600 nm), ◇; 4 mM (595 nm), × ; 8 mM (585 nm), +; 16 mM (580 nm), △; 32 mM (580 nm), ●; 64 mM (580 nm), ■; 128 mM (580 nm), ◆; and 256 mM (580 nm), ▲, respectively. The solid lines are the calculated curves. The conditions used for the sample solution were the same as those described in the caption of Figure 3.

eq 1 can be modified as follows:

$$DM-(NpHR^{blue})_m \rightarrow OG-(NpHR^{blue})_n \rightarrow I_{450} \rightarrow I_{380} \quad (2)$$

where subscripts m and n ($m > n$) denote the number of NpHR monomers in the assembly. Kinetic analysis of the two-dimensional contour map of the spectral changes was performed by a combination of the singular-value decomposition (SVD) approach and the global-fitting approach using a multiexponential function. On the basis of this analysis, three optimal rate constants, i.e., 0.114, 0.048, and 0.005 s^{-1}, were determined. Figure 5B shows the calculated two-dimensional contour map drawn by three-exponential fitting using the optimal rate constants. Figure 6 shows the curve fitting of absorbance changes at 600, 450, and 380 nm using these three rate constants. This fitting indicates that decreases from chloride-free $NpHR^{blue}$ to I_{450} and an increase from I_{450} to I_{380} were dominant, because the fraction of the fastest rate constant, 0.114 s^{-1}, which was attributed to the decrease in the assembling number of components for assembly between $DM-(NpHR^{blue})_m$ and $OG-(NpHR^{blue})_n$, accounted for only 5% of the total change at 600 nm. Thus, the medium and the lowest rate constants (i.e., 0.048 and 0.005 s^{-1}) were attributed to the formation of I_{450} and I_{380}, respectively.

Effects of Chloride and pH on the Bleaching of NpHR. It was found that the bleaching kinetics of NpHR because of the addition of OG depends upon the concentration of the chloride ion, as shown in Figures 3 and 4. This finding indicates that the equilibrium, chloride-bound NpHR ⇔ chloride-free NpHR, should be introduced for chloride-dependent bleaching. When the chloride concentration was higher than the chloride dissociation constant of NpHR (K_d = ~5 mM), there was a small amount of chloride-free NpHR. In this case, the transient I_{450} did not accumulate, and thus, the formation of I_{380} was slower than that of chloride-free NpHR (0.005 s^{-1}). When there was no chloride in the detergent system, all chloride-free NpHR changed to I_{380} through an I_{450} intermediate, as shown in eq 2.

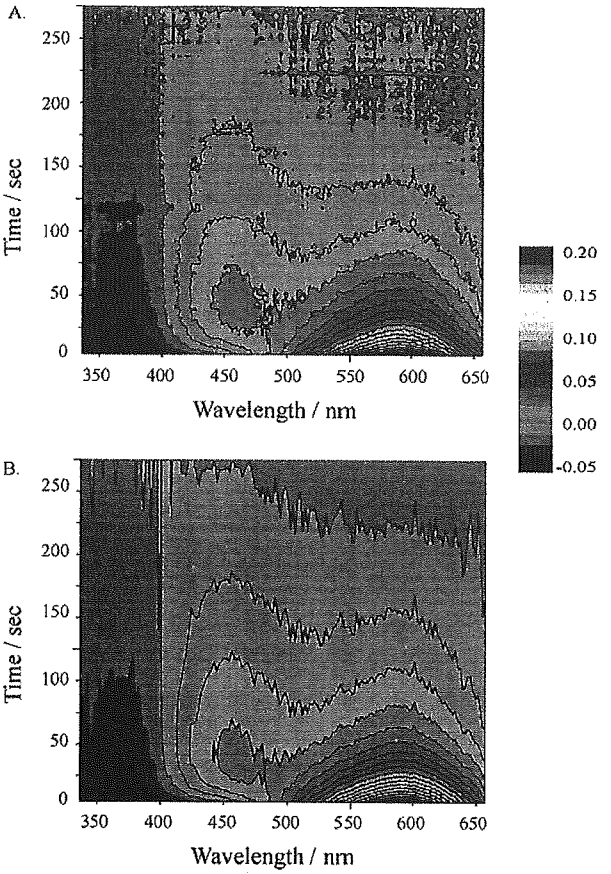

FIGURE 5: Observed (A) and calculated (B) two-dimensional contour maps of differential absorbance during the bleaching reaction of chloride-free DM−NpHR obtained from stopped-flow rapid-mixing experiments. The sampling interval and the total observation times were 1 and 250 s, respectively. Differential absorbance [Abs (t) − Abs (250 s)] was plotted. The calculated map was obtained from three-exponential fitting after the SVD analysis and the global fitting. The contour intervals of ΔAbs were 0.01. The final concentration of the mixed solution was 50 mM OG, 1 mM DM, and 10 mM MOPS (pH 7.0).

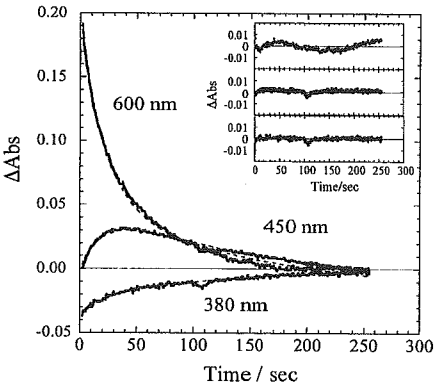

FIGURE 6: Absorption change at three wavelengths (380, 450, and 600 nm) based on the results shown in parts A and B of Figure 5 obtained during the bleaching reaction of NpHR in the absence of NaCl. The solid and broken lines show the observed and global-fitted data, respectively. The inset represents the residuals between the best-fit and the observed data.

On the other hand, to clarify the effects of pH on the bleaching process of NpHR, the spectral changes in NpHR by the addition of OG were measured at pH 1.5 (Figure 7).